Remote Sensing of Environment 329 (2025) 114927

Contents lists available at ScienceDirect

Remote Sensing of Environment

journal homepage: www.elsevier.com/locate/rse

Fusing SAR image and CYGNSS data for monitoring river water level changes by machine learning

Yan Jia [a], Quan Liu [a], Chunqiao Song [b,c], Zhiyu Xiao [a], Qiang Dai [d], Shuanggen Jin [e,f,g,*], Patrizia Savi [h]

[a] Department of Surveying and Geoinformatics, Nanjing University of Posts and Telecommunications, Nanjing 210023, China
[b] Key Laboratory of Watershed Geographic Sciences, Nanjing Institute of Geography and Limnology, Chinese Academy of Sciences, Nanjing 210008, China
[c] University of Chinese Academy of Sciences, Nanjing (UCASNJ), Nanjing 211135, China
[d] Key Laboratory of VGE of Ministry of Education, Nanjing Normal University, Nanjing 210023, China
[e] School of Surveying and Land Information Engineering, Henan Polytechnic University, Jiaozuo 454003, China
[f] Shanghai Astronomical Observatory, Chinese Academy of Sciences, Shanghai 200030, China,
[g] School of Artificial Intelligence, Anhui University, Hefei 230601, China
[h] Department of Electronics and Telecommunications, Politecnico di Torino, 10129 Torino, Italy

ARTICLE INFO

Editor name: Jing M. Chen

Keywords:
CYGNSS
Sentinel-1
GNSS-R
Water level
Machine learning

ABSTRACT

Accurate river water level estimation is essential for effective flood monitoring and water resources management. However, traditional techniques and single satellite observations have low accuracy and resolution. In this paper, we propose a novel method to enhance river water level estimation by fusing Cyclone Global Navigation Satellite System (CYGNSS) data and Sentinel-1 Synthetic Aperture Radar (SAR) imagery based on advanced machine learning (ML) techniques. SAR provides high-resolution, all-weather surface imagery, while the GNSS-Reflectometry from the eight-satellite CYGNSS mission offers frequent and wide-coverage observations. Dynamic river water levels are obtained at a daily temporal resolution by extracting changes in Sentinel-1 backscattering coefficients and integrating them with the CYGNSS data's high temporal resolution feature. To guarantee the model's robustness, a ten-fold cross-validation (CV) procedure is used with incorporating 15 uniformly distributed gauge sites. Experimental results show that the data fusion method significantly improved the temporal resolution, and more importantly the precision of water level estimation. As opposed to the model without data fusion, the optimized fusion algorithm achieved a 50.74 % reduction in RMSE from 0.341 to 0.168 m, while the R was improved from 0.876 to 0.936. An improvement of over 35 % in RMSE was observed at 8 out of 15 stations. To further validate the model's generalizability, we tested it using data from 8 spatially and temporally independent hydrological stations. The fusion method reduced the RMSE from 0.479 to 0.202 m and increased the R from 0.848 to 0.927, further confirming its effectiveness in enhancing water level estimation. The findings indicate that integrating SAR imagery and CYGNSS time series data has complementary effects and enables better water level estimation.

1. Introduction

River water levels, also known as river stages or river surface elevations, are a crucial indicator of the hydrological cycle. They form the primary basis for water resource management strategies and environmental protection (Dastour and Hassan, 2023; Hu et al., 2023; Zhou et al., 2023). Monitoring river water level changes in real-time is essential not only for water resource management, ecological environment assessment, climate modeling, and biodiversity research but also for providing decision-making support for policy formulation at local and national levels (Biswas et al., 2019). Traditional point-based water level measurement methods are simple to operate, while they no longer

Abbreviations: BJ, Banjing; BY, Baoying; BYB, Baoyingbao; CDP, Chuandong Port; DN, Dingnian; DT, Dongtai; DLP, Doulong Port; FC, Fanchuan; FN, Funing; GG, Gaogang; GY, Gaoyou; HQ, Huangqiao; JD, Jiangdu; JHu, Jianhu; JHe, Jinghe; MD, Mangdao; SD, Sanduo; SYT, Sheyang Town; TZ, Taizhou; XH, Xinghua; YC, Yancheng; YL, Yiling; ZB, Zhongbao.

* Corresponding author at: School of Surveying and Land Information Engineering, Henan Polytechnic University, Jiaozuo 454003, China
E-mail addresses: sgjin@shao.ac.cn, sgjin@hpu.edu.cn (S. Jin).

https://doi.org/10.1016/j.rse.2025.114927
Received 4 September 2024; Received in revised form 16 July 2025; Accepted 16 July 2025
Available online 25 July 2025
0034-4257/

meet the demands of modern, large-scale, real-time monitoring, exhibit the reduced reliability in harsh environments, and entail high maintenance costs.

Satellite remote sensing (RS) has proven to be an essential tool for inland hydrological monitoring and study worldwide (Koblinsky et al., 1993; Alsdorf et al., 2007; Calmant et al., 2008; Crétaux et al., 2011). These observations measure a range of hydrological variables such as wetland areas (Papa et al., 2010), streamflow in major rivers (Birkett, 1998; Birkett et al., 2002; Frappart et al., 2005; Frappart et al., 2008; Papa et al., 2006), and water levels in floodplains, lakes, wetlands, and rivers as observed by different satellite missions (Calmant et al., 2008; Pandey et al., 2014; Tarpanelli et al., 2018).

Various types of images captured by satellite optical sensors, including the Moderate Resolution Imaging Spectroradiometer (MODIS) with resolutions of 250 m and 500 m, Landsat with a 30-m resolution, and Sentinel−2 with a 10-m resolution, have been utilized to monitor changes in lake water bodies (Lu et al., 2013; Xu et al., 2020; Wu et al., 2023). The Modified Normalized Difference Water Index (MNDWI) and Normalized Difference Water Index (NDWI) (McFeeters, 1996; Li et al., 2021) are the two most utilized multispectral indices for monitoring changes in water surfaces. Water bodies are usually extracted using higher values of NDWI and MNDWI (Pham-Duc et al., 2017). However, optical imagery is sensitive to cloud occlusion, which significantly impacts the usability and accessibility of optical image data (Kleinherenbrink et al., 2020; Kushwaha et al., 2022). In comparison with optical RS, radar RS offers the benefit of penetrating clouds, rain, and fog, thus enabling all-day, all-weather observation without being affected by weather conditions (Zhang et al., 2011; Ferrentino et al., 2020; Hamunyela et al., 2022). The category includes radar altimetry (RA) and synthetic aperture radar (SAR), among others.

RA approaches have been used to monitor changes in water levels of terrestrial water bodies, utilizing platforms such as ICESat-1/2, Sentinel-3, Jason-1/2/3, and CryoSat, along with digital elevation models (DEMs) (Birkett et al., 2002; Huang et al., 2018; Li et al., 2019b; Ryan et al., 2020; Cooley et al., 2021; Garkoti and Kundapura, 2021; Parajuli et al., 2022; Yue et al., 2022; Song et al., 2023). Data from multiple altimetry missions have been used in many studies to compile global water level datasets. For instance, the Database for Hydrological Time Series of Inland Waters (DAHITI) integrates altimetry data from SARAL/AltiKa, Envisat, Jason-1/2, TOPEX/Poseidon, and ERS-2, comprising thousands of time series of water levels for wetlands, lakes, reservoirs, and rivers (Schwatke et al., 2015). DEM data are frequently used to supplement and calculate water level values in cases where altimetry information is limited (Vanthof and Kelly, 2019; Weekley and Li, 2021). However, aside from a few exceptions, altimeter methods presently face limitations in spatial resolution. They are primarily suitable for large lakes and water bodies beneath orbital paths, and thus cannot cover many small lakes and rivers globally (Alsdorf et al., 2007; Hostache et al., 2009; Sulistioadi et al., 2015; Mohammadimanesh et al., 2018).

SAR is broadly utilized for monitoring surface water owing to its insensitivity to clouds and sunlight. The C-band SAR, including Envisat, Radarsat, ERS-1, and ERS-2, builds on the legacy of traditional SAR systems developed by ESA and Canada (Santoro et al., 2015). Sentinel-1 data have been widely adopted worldwide, showcasing significant potential for monitoring surface water with high resolution (Ferrentino et al., 2020; Palomino-Ángel et al., 2022). However, the establishment of water level estimation solely from SAR data is significantly limited due to insufficient observational data and challenges in temporal resolution (*e.g.*, a 6-day observation cycle in northern regions) (Iervolino et al., 2014; Pham-Duc et al., 2017; Xing et al., 2018). Unlike traditional SAR satellites, the Surface Water and Ocean Topography (SWOT) satellite, successfully launched in December 2022, is the first satellite specifically designed to measure surface water changes (Fu et al., 2012). It uses dual-frequency (Ka and Ku bands) near-nadir SAR interferometry, combining the advantages of radar altimetry (for water level detection) and high-resolution SAR imagery, enabling the acquisition of key parameters such as river width and water level. SWOT's observation range is extensive, covering rivers wider than 100 m and lakes or reservoirs with a surface area of at least 250 m × 250 m, spanning a geographical range from 78°S to 78°N. With a 21-day revisit period, SWOT offers new opportunities for monitoring wider rivers and larger lakes, as well as supporting long-term hydrological studies. (Durand et al., 2010; Altenau et al., 2021; Pavelsky et al., 2014).

Global Navigation Satellite System Reflectometry (GNSS-R) leverages satellite signals bounced back from Earth's surface to evaluate surface parameters, which is a passive bistatic radar method (Wang et al., 2018; Yan et al., 2020; Jia et al., 2024a; Jia et al., 2024b; Jin et al., 2024; 5aJin et al., 2025a; Jin et al., 2025b). Martin-Neira (1993) initially proposed the GNSS-R altimetry, utilizing the time delay of reflected signals along with the predetermined geographical points of the transmitter and receiver to estimate the reflecting surface height. Subsequent research has demonstrated its value in altimetry studies based on space, airborne, and ground platforms (Treuhaft et al., 2001; Lowe et al., 2002a; Clarizia et al., 2016; Li et al., 2019a; Wang et al., 2021; Ye et al., 2022; Roesler et al., 2023), leading to rapid development. Early GNSS-R altimetry studies utilized only limited surface reflection data (Lowe et al., 2002b). However, the Cyclone Global Navigation Satellite System (CYGNSS) Earth Explorer project, established by the National Aeronautics and Space Administration (NASA) in 2016 (Ruf et al., 2018), provides a substantial amount of long-term observational data for GNSS-R altimetry research (Zhang and Morton, 2023).

The CYGNSS satellites were originally intended to study ocean surface winds during tropical cyclones, which generate delay-Doppler maps (DDMs) by measuring Doppler shifts along with delay in the returned signal through cross-correlation between local reference signals and the received reflected signals. Based on the derived DDMs along with surface reflection measurements, three common observables can be estimated for GNSS-R altimetry applications: a blend of pseudorange and carrier phase measurements, a combination of carrier phase observations, and the signal-to-noise ratio (SNR).

In comparison with traditional RA, several benefits, such as reduced instrument power requirements, the capability to simultaneously gather measurement data from various GNSS satellites for wider coverage, and higher temporal resolution, are provided by spaceborne GNSS-R altimetry (Xi et al., 2022). Larson et al. (2013) carried out a pioneering water level retrieval experiment to infer sea level fluctuations using GPS data collected at a site from the EarthScope Plate Boundary Observatory (PBO). This method removed direct signal interference from raw SNR measurements using low-order polynomial fitting and reduced noise using wavelet decomposition (Santamaría-Gómez et al., 2015; Santamaría-Gómez and Watson, 2017; Wang et al., 2019b). Other SNR-based research has shown the applicability of multi-constellation and multi-frequency GNSS signal SNR data in GNSS-R, showing that multi-GNSS signal combinations yield better retrieval results than single-GNSS signals (Löfgren et al., 2011; Wang et al., 2019a).

Whilst the technologies described above have allowed major progress in the area of hydrological remote sensing, several issues remain, including low spatial resolution (*e.g.*, Jason series, GRACE), long revisit cycles (*e.g.*, SWOT), and limited applicability to complex terrains such as dense water networks. Furthermore, certain satellites (*e.g.*, Landsat, MODIS) can only infer water levels indirectly through water body extent analysis, lacking the capability for direct water level measurement. These shortcomings directly restrict their effectiveness in key applications such as small watershed hydrological monitoring, flood forecasting, eco-hydrological research, and disaster emergency response. Data fusion technology offers a promising solution by integrating the strengths of multiple data sources, thereby overcoming the constraints of individual systems. Unlike our previous work and that of others, here we present a novel framework that unifies the representations of SAR images and CYGNSS data, leveraging their complementary strengths. The approach explicitly addresses the challenges of high spatiotemporal resolution, cost efficiency, and broad coverage, enabling direct and

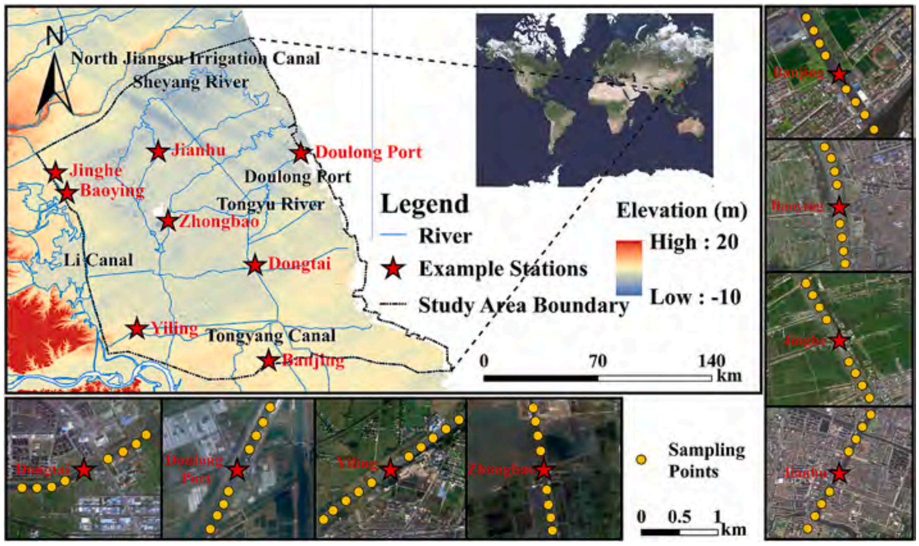

Fig. 1. Location of the study area and sampling locations. The map on the left shows the distribution of rivers and stations in the study area (Black text: names of rivers), and the map on the right shows the geographical location of the study area, the eight inset maps display the geographic extent and specific sampling points of the eight hydrological sites used for spatially and temporally independent testing.

dynamic water level monitoring. This technology fills the gaps in existing water level satellites in terms of high-frequency and high-precision monitoring, particularly suitable for small-scale water body monitoring, flood warning, and emergency response applications. It provides a more powerful tool for hydrological research and disaster management.

From a technical perspective, our primary objective aims to determine whether fused SAR and CYGNSS data features are sensitive to water level changes and can improve the accuracy of water level estimation. Our framework offers two key potential advantages: (1) Stable and consistent features can be extracted from heterogeneous data. (2) It is possible to bridge the differences between datasets and generate high spatial-temporal resolution data series, thereby improving the model's robustness and its capacity to withstand interference.

Our primary contributions are summarized as follows:

(1) A novel spatiotemporal fusion method was proposed for river water level estimation by combining SAR images and CYGNSS data, which produces daily high spatial-resolution features and achieves higher accuracy.

(2) Different ML algorithms and feature combinations were evaluated to measure the effectiveness of the suggested approach.

2. Study area and datasets

2.1. Study area

The Lixiahe region (latitude 32° to 34° 30′ N, longitude 119° to 121° 30′ E) is located in central Jiangsu Province, China, covering approximately 22,000 km^2 (see Fig. 1). The terrain is low and relatively flat, with elevations below 3 m accounting for 80.2 % of the area, referred to as the "pot bottom depression." As a typical low-lying and coastal area, Lixiahe is particularly vulnerable to both flooding and drought disasters due to its unique geographical and climatic characteristics. The region experiences frequent and intense rainfall during the Meiyu season in spring and summer, as well as heavy rains induced by typhoons in summer and autumn, which ranks it among the regions that are most susceptible to disasters worldwide (Jiang et al., 2024). As a representative floodplain river system region, Lixiahe exhibits geographical characteristics common to many areas worldwide, such as slow water flow, dense river networks, and numerous lakes, making water level monitoring studies in this region highly valuable for other plain areas globally. Additionally, the region's subtropical monsoon climate, with its seasonal rainfall patterns and water level fluctuations, is representative of many mid- to low-latitude regions. The study of Lixiahe's distinct hydrological and topographical features provides valuable insights for global water resource management and flood disaster prevention in other densely river-networked plains.

Fig. 1 shows the location of the study area and marks the distribution of the key stations within the scope of this study, including the eight stations selected for spatially and temporally independent testing.

2.2. CYGNSS dataset

The CYGNSS constellation is composed of eight microsatellites (Ruf et al., 2018; Li et al., 2023b). Each microsatellite is equipped with a bistatic radar receiver with four channels designed to capture GPS signals that bounce off the Earth's surface. The microsatellites primarily operate in equatorial regions, spanning from 38° N to 38° S. In contrast to sun-synchronous satellites with revisit times ranging from one to three days, such as SMAP and SMOS, CYGNSS offers a significantly higher temporal resolution, achieving an overall revisit time of just a few hours (Ruf et al., 2016). The reflection points and the surface roughness in its vicinity influence the spatial resolution of the CYGNSS signals. For active scattering from smooth surfaces, the spatial resolution can reach 0.5 km (Comite et al., 2019).

The GPS signals that bounce off the Earth's surface are recorded to produce delay-Doppler maps (DDMs). These DDMs are processed to derive the bistatic radar cross section (BRCS) along with the effective scattering area corresponding to each specular point by inverting the forward scattering model of CYGNSS. The BRCS from CYGNSS is arranged in a 17-delay by 11-Doppler grid, providing a representation of the radar reflectivity.

This study utilizes the CYGNSS level 1 version 3.1 data product, which is freely available (https://podaac.jpl.nasa.gov/CYGNSS) from January 1, 2021 to October 31, 2023. The BRCS is represented as P_{brcs}. $\Gamma_{x,y}$, surface reflectivity, can be derived from the calibrated DDM peak with these level 1 observations (Rodriguez-Alvarez et al., 2019) as follows:

$$\Gamma_{x,y} = \frac{(r_{st} + r_{sr})^2}{4\pi(r_{st}r_{sr})^2} P_{brcs} \tag{1}$$

where r_{st} represents the distance between the specular reflection point

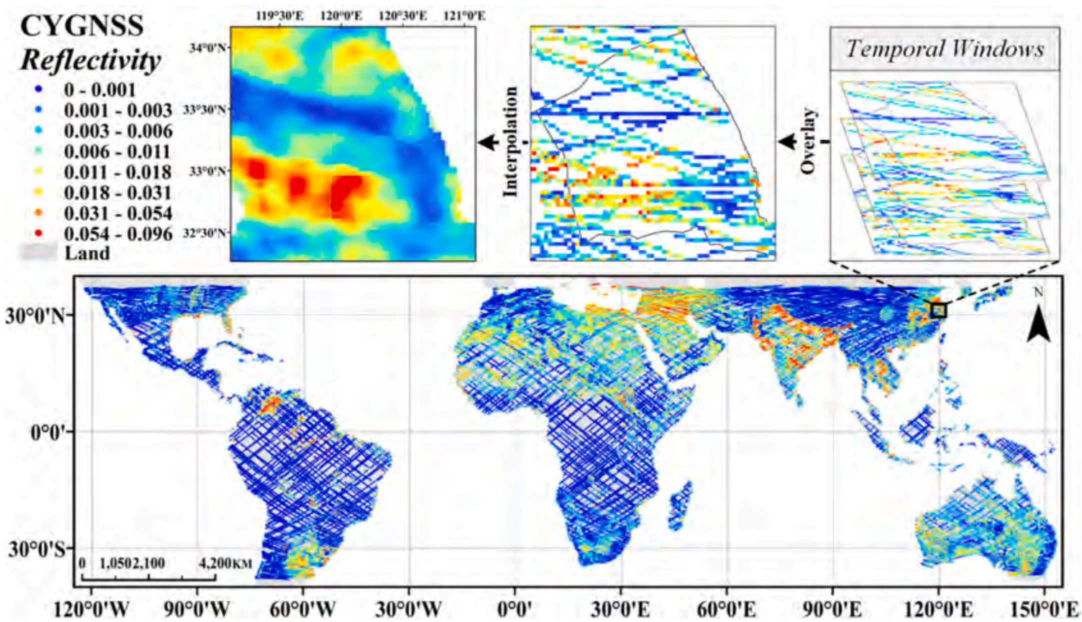

Fig. 2. Sample map of surface reflectivity data extracted from CYGNSS (2022.1.1).

and the satellite system transmitter, and r_{sr} denotes the distance from the receiver to the specular reflection point. Due to the variable positions of CYGNSS data sampling points, the calculated surface reflectivity data are typically projected onto a specific resolution (*e.g.* 36 km) EASE 2.0 grid, as shown in Fig. 2. To ensure the accuracy and reliability of the data, multiple quality control measures were performed on the data (Jia et al., 2021). For example, the reflectivity data obtained from CYGNSS were filtered using the incident angle and DDM characteristics to remove outliers. Meanwhile, we employed a three-day time sliding window strategy and Kriging interpolation method to fill and smooth the gaps in the CYGNSS data caused by the relatively random sampling points and discontinuous spatial coverage (Shepard, 1968; Luo et al., 2023; Senyurek et al., 2021; Senyurek et al., 2022).

2.3. Sentinel-1 SAR dataset

Sentinel-1 is the essential element within the Copernicus program. It primarily consists of two satellites, Sentinel-1 A and Sentinel-1B, both equipped with advanced SAR systems that provide all-weather, all-time radar imagery. Each satellite completes an orbit every 12 days, and together, the two-satellite constellation achieves a global revisit period of 6 days. The Sentinel-1 sensor functions in four distinct modes: wave (WV) mode, stripmap (SM) mode, interferometric wide swath (IW) mode, and extra-wide swath (EW) mode. The default mode for Earth observations is the IW mode, providing both single-band polarizations (VV, VH) and dual-band polarizations (VV + VH, HH + HV).

This study employed the VV + VH dual polarization combination with a spatial resolution of 5 × 20 m. A total of 657 Sentinel-1 A SAR images in IW mode with dual-band polarizations (VV + VH) were collected. These level-1 ground range detected (GRD) images, covering

Table 1
Stations utilized for validating the proposed method.

Name	River	Longitude (°)	Latitude (°)	Elevation (m)	Slope (°)	Water level range (m)	Average water level (m)
Banjing	Jiaogang River	120.41	32.31	5	2.18	2.08–4.01	2.48
Baoying	Li Canal	119.31	33.24	4	3.62	6.02–7.77	6.75
Baoyingbao	Baoshe River	119.52	33.26	1	2.18	0.62–2.40	1.07
Chuandong Port	Chuandong Port	120.8	33.05	1	0	0.40–1.50	1.00
Dingnian	Tongyang Canal	120.7	32.36	4	2.9	2.08–3.28	2.45
Dongtai	Taidong River	120.34	32.83	4	4.41	0.92–2.50	1.20
Doulong Port	Doulong Port	120.59	33.46	2	3.9	0.85–1.87	1.26
Fanchuan	Xiefeng River	119.69	32.67	3	1.62	1.07–2.02	1.40
Funing	Sheyang River	119.78	33.78	1	2.05	0.41–1.60	0.89
Gaogang	Yinjiang River	119.84	32.32	0	2.05	0.69–2.52	1.44
Gaoyou	Li Canal	119.42	32.79	4	3.62	5.85–7.76	6.81
Huangqiao	Laolong River	120.22	32.26	5	2.99	2.14–4.68	3.10
Jiangdu	New Tongyang Canal	119.57	32.42	1	0.73	0.11–3.16	1.52
Jianhu	Xitang River	119.8	33.47	3	1.62	0.17–2.40	0.94
Jinghe	Li Canal	119.23	33.35	13	3.62	6.03–7.80	6.74
Mangdao	Mangdao River	119.55	32.42	1	3.9	5.78–8.20	6.88
Sanduo	Beichengzi River	119.65	32.82	2	1.62	1.01–2.12	1.35
Sheyang Town	Sheyang Lake	119.61	33.3	3	3.62	0.41–2.37	1.06
Taizhou	Tongyang Canal	119.92	32.48	1	2.29	2.06–2.92	2.52
Xinghua	Nanguan River	119.83	32.93	3	0	1.03–2.26	1.32
Yancheng	Chuanchang River	120.12	33.4	9	2.18	0.61–1.86	1.01
Yiling	New Tongyang Canal	119.68	32.49	1	4.58	0.62–2.74	1.43
Zhongbao	Wugong River	119.84	33.09	-2	0	0.86–2.75	1.16

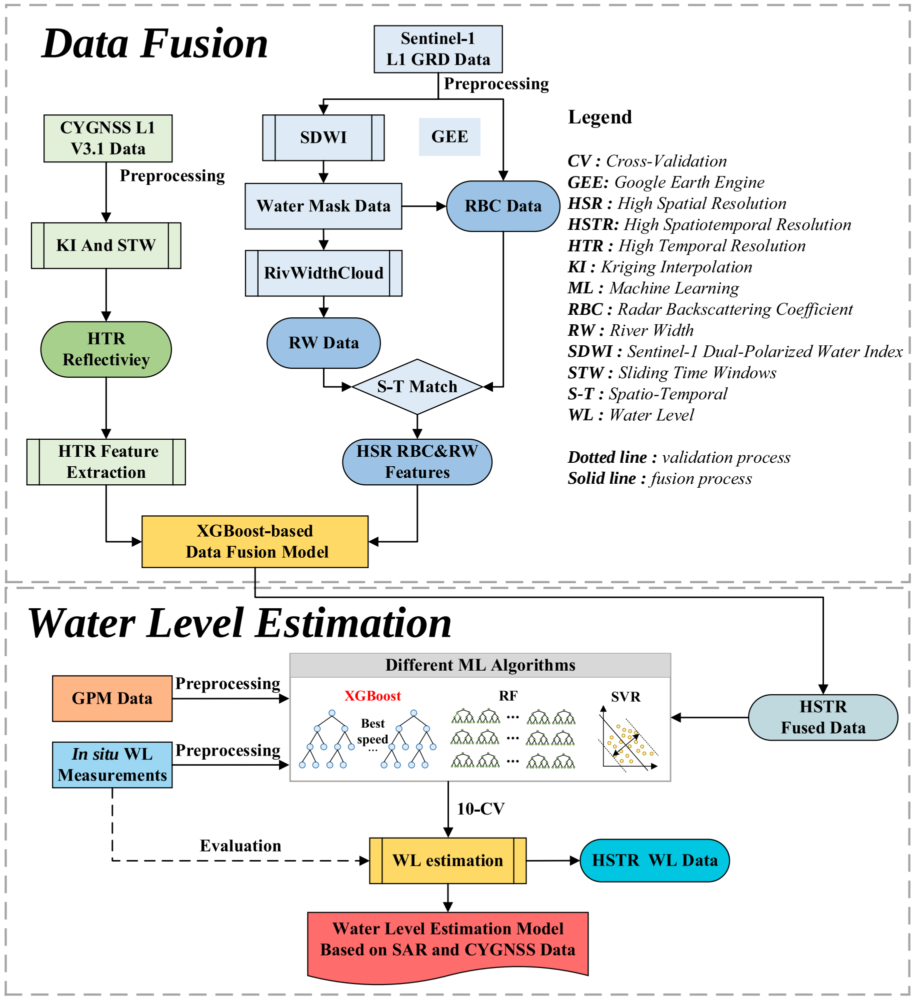

Fig. 3. Study flowchart.

the period from January 1, 2021, to October 31, 2023, were obtained from the Google Earth Engine (GEE).

The dataset underwent a series of preprocessing steps to derive the backscatter coefficient for each pixel (Dastour et al., 2022). The obtained radar backscatter coefficient data include the central coordinates of the observation location (longitude and latitude {X, Y}) and the radar backscatter coefficient at the observation point $\sigma^0_{x,y}$. The radar backscatter coefficient can be calculated with the following equation:

$$\sigma^0_{x,y} = f(\lambda, \theta, P) \cdot g(\varepsilon_\gamma, s_r, s_c) \tag{2}$$

where include wavelength λ, incidence angle θ, and polarization mode P. The target parameters include complex dielectric constant ε_γ, surface roughness s_r, and volume scattering coefficient s_c in heterogeneous media.

Additionally, to minimize the impact of coherent speckle noise and terrain variations, this study adopted the Lee filter method and a volume scattering-based terrain correction model (Lee, 1980). All available data were processed on the GEE platform to leverage its powerful computational resources and advanced processing tools.

2.4. GPM dataset

Led by the Japan Aerospace Exploration Agency along with NASA, the Global Precipitation Measurement (GPM) project builds upon the Tropical Rainfall Measuring Mission through a collaborative effort. Since March 2014, the GPM project has been delivering the Level 3 Integrated Multi-satellite Retrievals for GPM (IMERG) product, which provides advanced rainfall observation data with a spatial resolution of 0.1° and a temporal resolution of 30 min (Hou et al., 2014). The data is available through NASA's Goddard Space Flight Center data center (https://disc.gsfc.nasa.gov/datasets/GPM_3IMERGDE_06/summary). Here, GPM data were selected as an auxiliary input for the water level estimation modeling, given the relationship between rainfall and water levels. We applied nearest-neighbor interpolation to align the data with the other datasets.

2.5. In situ water levels

The observational data for this study included daily *in situ* water level data collected between January 2021 and October 2023, which are freely available from the National Water and Rainfall Information website (http://xxfb.mwr.cn/sq_dtcx.html?v=1.0). Twenty-three representative stations with high data integrity were chosen for this study. The morphological attributes and topographic properties of these stations are presented in Table 1 and Figure 1with the diverse morphological characteristics of the region's rivers.

Despite the daily recordings, some data gaps existed due to incomplete records and potential issues with network transmission. Nevertheless, this dataset was valuable for developing and validating the accuracy of the model employed for water level estimation.

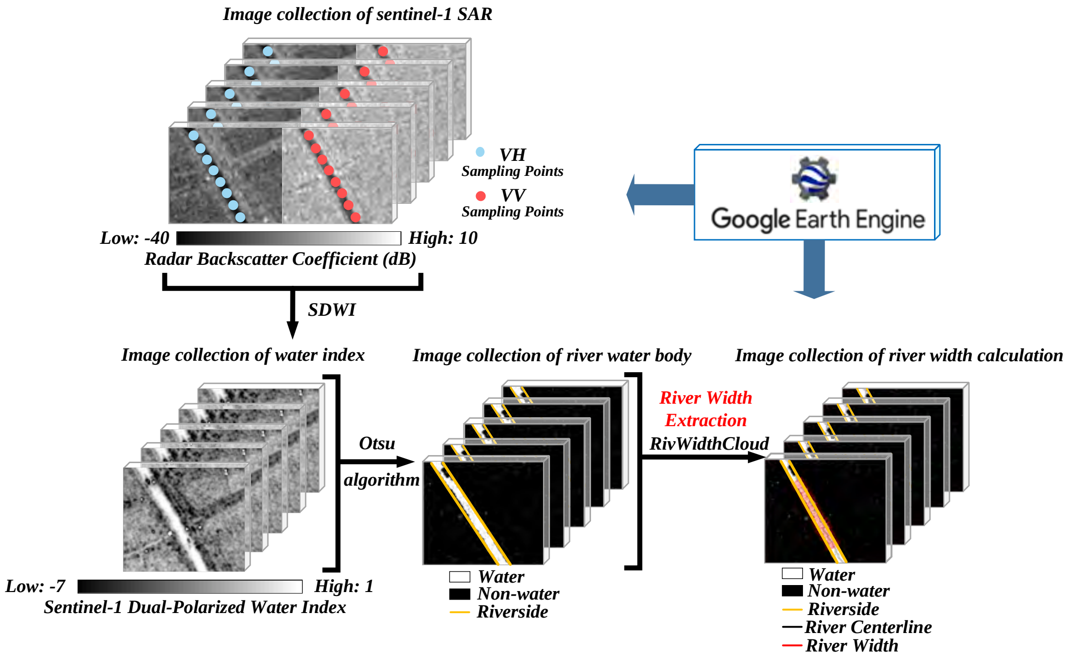

Fig. 4. Process for extracting Sentinel-1 imagery features (river width and backscattering coefficient) implemented based on the Google Earth Engine.

3. Methodology and procedures

This study proposed a new framework that unifies SAR images and CYGNSS data representations, leveraging ML techniques to improve the sensitivity and complementary effects of water level monitoring. Additionally, our approach ensured stable feature extraction from diverse data sources and bridged differences between datasets to generate high-spatiotemporal water level estimations.

3.1. Overall framework

We developed a high spatiotemporal resolution water level estimation model (~1 day) using Sentinel-1, CYGNSS, and ancillary data during 2021–2023 (see Fig. 3). First, Sentinel-1 imagery, CYGNSS, and other ancillary data were acquired and preprocessed. CYGNSS data were cleaned and spatially augmented using a three-day time sliding window and Kriging interpolation to provide high coverage. The SDWI (Sentinel-1 Dual-polarized Water Index) algorithm was used to detect water bodies in the Sentinel-1 backscatter coefficient images and to calculate geometric parameters such as river width.

A critical aspect of the methodology was the feature fusion of Sentinel-1 and CYGNSS data, combining CYGNSS's high temporal resolution with Sentinel-1's high spatial resolution. Specifically, high temporal resolution statistical features from CYGNSS were extracted and applied to Sentinel-1 data using ML algorithms to obtain continuous fusion features with high spatiotemporal resolution (see details in Section 3.3).

The fused features from CYGNSS and Sentinel-1 data, including GPM data, were employed to develop an ML-based water level model using *in situ* measurements from 15 uniformly distributed gauge sites. Multiple ML algorithms were used to train the model, ensuring robustness through a 10-fold cross-validation (CV) method. Additionally, *in situ* data from eight spatiotemporally independent stations were used to evaluate the model's accuracy. Thus, by integrating Sentinel-1 SAR imagery and CYGNSS data, a high spatiotemporal resolution water level monitoring model was developed, resulting in accurate water level estimation.

3.2. Extracting high-spatial resolution features from Sentinel-1 images

The low backscatter characteristics of water bodies in the microwave range, due to the specular scattering effects, provide the basis for water extraction in Sentinel-1 images (Grimaldi et al., 2020; Martinis et al., 2022; Chen et al., 2024). Specifically, the surface roughness due to water level changes can further influence SAR backscatter coefficients over water surfaces. Increased water surface roughness complicates the scattering phenomenon, as the irregular surface causes electromagnetic waves to scatter in a broader range of directions and angles. This affects the intensity and distribution of the scattering. VH and VV polarized radar backscatter coefficients are responsive to changes in water levels, with each type exhibiting a different degree of sensitivity. Different polarizations carry distinct information, enhancing the correlation for water estimation. Consequently, the variation of the Sentinel-1 backscatter coefficients can be used to reflect water level changes. The spatial variations in backscatter coefficients can provide valuable information and assist in disentangling the effects of additional surface factors (Santoro et al., 2015).

In addition to the key feature of the backscatter coefficient, river width can also visually demonstrate changes in river water levels. The river water spreads to a broader area when the water level rises, causing the river width to increase; conversely, the river width decreases when the water level falls. This phenomenon is especially significant in natural river channels where the terrain on either side of the river is fairly flat. Therefore, monitoring changes in river width can indirectly infer changes in river water level.

To accurately obtain the river width and backscatter coefficient from Sentinel-1 images, the following key steps were used (See Fig. 4): First, we calculated the SDWI derived from grayscale attributes associated with water bodies in different polarization SAR images using Sentinel-1 dual-polarization VV and VH bands (Guo et al., 2021; Li et al., 2023c; Xue et al., 2021). Then, this study employed Otsu's method, a classic and widely used approach for image segmentation, to segment the SDWI images and accurately extract water body information (Cordeiro et al., 2021; Garg et al., 2024; Yang et al., 2018; Young et al., 2024).

The imagery dataset used in this study was extensive, making manual extraction of features such as river width and backscatter coefficient from individual images both time-consuming and impractical. To

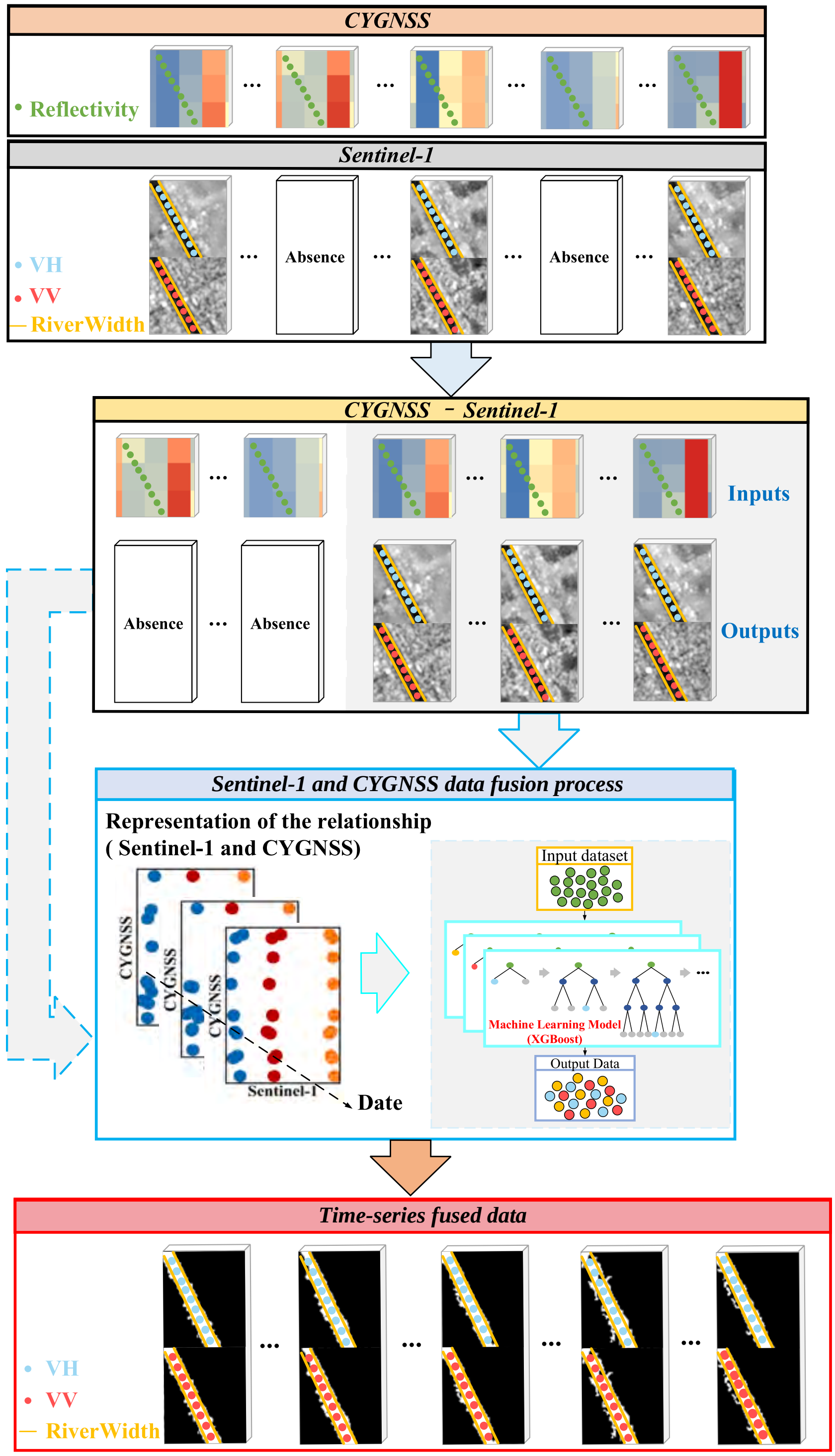

Fig. 5. General framework of the implemented temporal-spatial feature fusion modeling from CYGNSS and Sentinel-1 data for water level estimation.

address this, we employed batch-processing techniques and developed automated algorithms on the Google Earth Engine platform to enable rapid image analysis and feature extraction (Yang et al., 2020).

The precise river width calculation employed the RivWidthCloud algorithm after extracting water body masks (Yang et al., 2020). The core steps are summarized as follows:

(1) River Centerline Extraction: The centerline was generated by applying distance transformation, gradient calculation, and skeletonization techniques to the river mask, and false branches were removed to ensure accuracy.

(2) River Width Measurement: The local orthogonal direction for each pixel on the centerline was calculated and the river width along these directions was measured for comprehensive coverage.

The backscattering coefficient and river width are averaged within a 250-m radius buffer zone. Specifically, for each sampling point, we calculate the average values of the backscattering coefficient and river width within a 250-m radius buffer zone (considering only water bodies) centered at that point. This approach takes into account the diverse river morphology in the target area, ensuring coverage of the widest river sections while maintaining sampling consistency. By smoothing the data

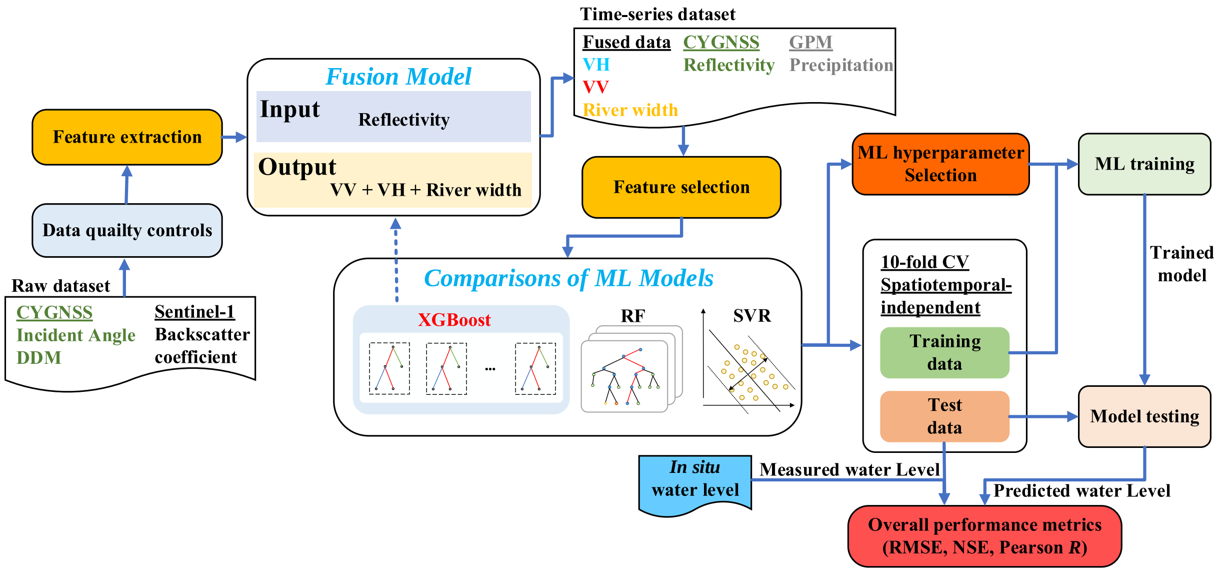

Fig. 6. Flowchart showing the training and validation of the proposed ML-based water level estimation method.

within the buffer zone, we reduce the impact of outliers, thereby enhancing the stability and reliability of the data.

3.3. Fusing Sentinel-1 images and CYGNSS data

In this study, we considered two main aspects when designing the fusion framework. First, it was important for the framework to be mathematically simple, robust, and computationally efficient. Given that the fusion process utilizes ancillary data and was executed for each pixel sequentially, simplicity and efficiency were crucial. Fig. 5 provides an overview of our proposed data fusion framework. Our approach assumed that key features obtained from different RS platforms should exhibit high consistency or linear correlation when observing the same region simultaneously.

First, high temporal statistical features from CYGNSS data with complete spatial distribution and continuous temporal sequences, specifically the daily change of reflectivity, were extracted to capture time-series variations. Simultaneously, spatial features from Sentinel-1 data, including the backscattering coefficients and river width data, were extracted to provide high spatial resolution imagery. Next, the temporal variation characteristics from CYGNSS were applied to the Sentinel-1 data, effectively supplementing the backscattering coefficients and integrating the temporal features with the spatial features of Sentinel-1. This integration involved establishing a pixel-level relationship between the two temporally overlapping datasets and using the XGBoost algorithm to solve the corresponding relationship. Finally, the solved and established model was applied to the discontinuous Sentinel-1 data, creating a synthetic data product that integrated the CYGNSS's high temporal resolution with the Sentinel-1's high spatial resolution. This synthetic product was then used for precise water level estimation modeling based on ML methods, utilizing *in situ* water level data for training and validation. The comprehensive experiments in Section 4 validated the effectiveness of the proposed method, demonstrating significant improvements in both temporal resolution and estimation accuracy.

3.4. ML framework for river water level estimation

Three machine learning (ML) algorithms, the support vector regression (SVR), extreme gradient boosting (XGBoost), and random forest (RF) algorithms, were selected for modeling and evaluating the proposed approach. The RF algorithm is widely used for its strong regression capabilities. XGBoost was chosen for its superior performance, speed, and robustness. SVR, known for its strong generalization ability, was also included to ensure a comprehensive comparison (Jia et al., 2024a; Li et al., 2023a).

Fig. 6 represents the process involved in the fusion and modeling of data using ML algorithms. First, we fused the extracted key features, including reflectivity from CYGNSS, backscatter coefficients and river width from Sentinel-1. The XGBoost algorithm was utilized to establish pixel-level correlations between the datasets. Specifically, the model was trained to express the relationship between temporally overlapping CYGNSS and Sentinel-1 data. Through this model, missing Sentinel-1 data could be supplemented, thereby forming a continuous and

Table 2
Hyper-parameters of ML learning algorithms.

XGBoost		RF		SVR	
parameter	value	parameter	value	parameter	value
booster	gbtree	*n_estimators*	200	*kernel*	rbf
objective	reg:squarederror	*max_depth*	15	*C*	100
n_estimators	150	*max_features*	sqrt	*gamma*	0.01
learning_rate	0.1	*min_samples_split*	5	*epsilon*	0.1
max_depth	6	*min_samples_leaf*	3		
gamma	0	*random_state*	42		
min_child_weight	3				
subsample	0.85				
colsample_bytree	0.8				
reg_alpha	0.01				
reg_lambda	0.1				

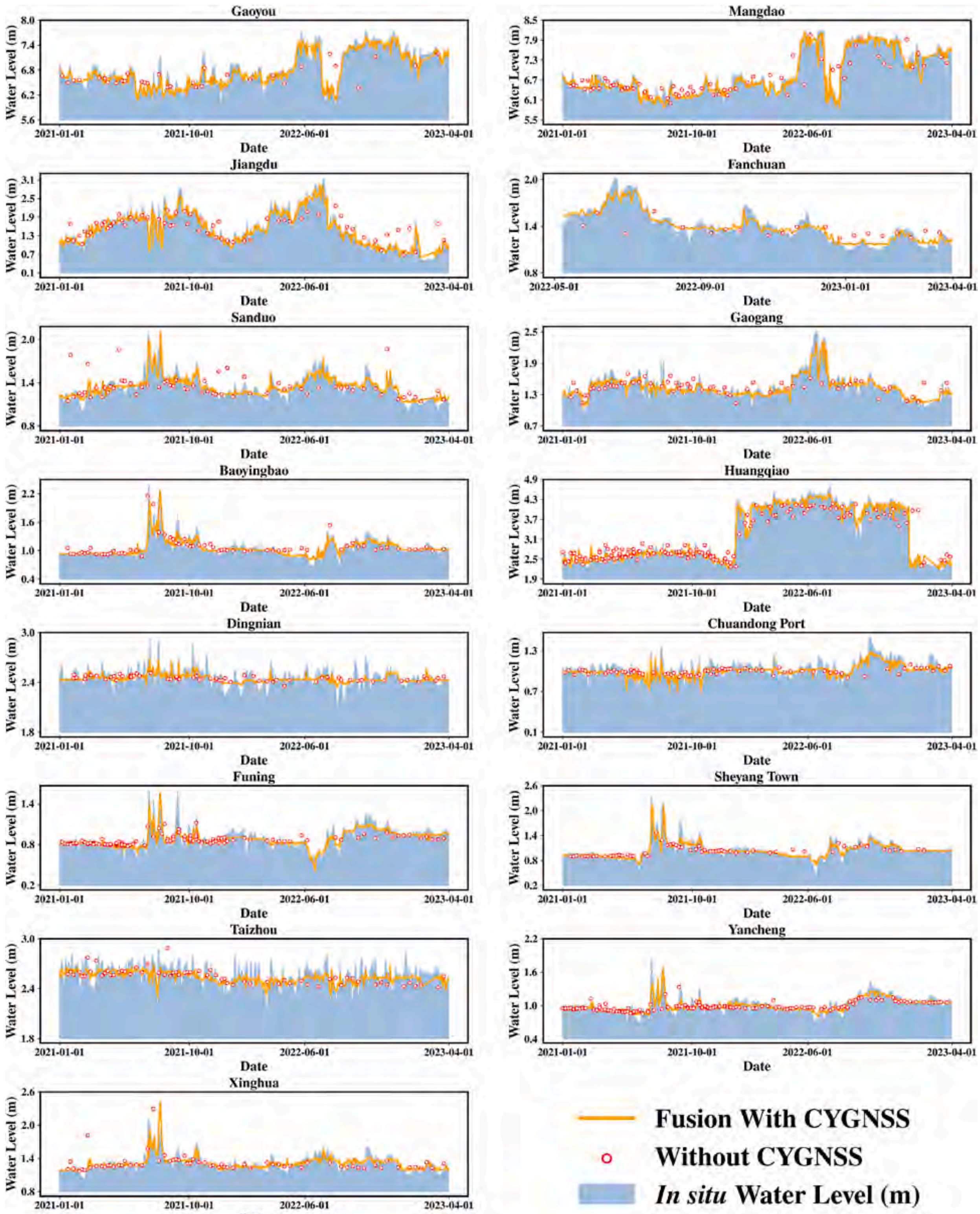

Fig. 7. Temporal variations of water level estimation with and without CYGNSS fusion at 15 stations based on 10-CV results.

complete fused dataset that combined the high temporal resolution of CYGNSS with the high spatial resolution of Sentinel-1.

Subsequently, the fused data and other optimized auxiliary features were selected to construct the water level estimation model. To evaluate the impact of various input features on the water level estimation, we conducted feature selection and optimization for the model inputs. Based on parameters such as date and geographical coordinates, we selected river width, backscatter coefficients (VV and VH), precipitation, and daily average reflectivity as the primary feature variables. These variables, along with observed water level data, were used to establish a river water level estimation model. The optimized features were evaluated based on three ML models, XGBoost, RF, and SVR algorithms. Finally, through comprehensive analysis of accuracy metrics, the optimal XGBoost-based model for water level prediction was determined, providing effective support for the dynamic monitoring of river water levels. Hyperparameters define the training and usage of a model, significantly influencing its complexity and fitting ability (Putatunda and Rama, 2018). The final selected hyper-parameters are shown in Table 2.

3.5. Validation strategy

In this paper, four ML-based methods were selected for comparison. ML models tend to use a standard framework of 1) training data used to train the model; 2) validation data used to tune the model; and 3) test data. This is required to keep some generalization capabilities and to avoid the so-called overfitting that is reserved from training and validation, and is only used to assess the test accuracy of the final model. The expected standard is that the test data have some independence from the training data (*i.e.*, different site and/or different time period) to reduce the impacts of spatial and temporal autocorrelation on assessed test accuracy.

For general validation, we adopted 10-fold CV on the dataset (from 2021 to 01-01 to 2023-03-31) to randomly access the overall model performance, which randomly selects 90 % of the samples for modeling and uses the remaining 10 % for validation (Senyurek et al., 2020; Bao et al., 2024). This process is repeated 10 times to ensure that all samples are tested. The final evaluation result is the average result of each fold. This approach inherently includes validation set partitioning, as each fold serves as validation data in turn, guaranteeing the separation of training and validation data while testing every fold. Different metrics are computed across all folds to evaluate the model performance, and the optimal model was selected based on its validation performance.

For a final test to rule out bias from the hyperparameter tuning, we tested the performance using an independent dataset not used for model design/tuning. This test was performed across different spatial and temporal dimensions to thoroughly evaluate the performance of the fused water level estimation model. As detailed in Section 4.3, we performed a spatiotemporally independent validation using data (from 2023 to 04-01 to 2023-10-31) to rigorously examine the model's generalization capability (Senyurek et al., 2020). Our evaluation framework incorporated both 10-fold CV and independent testing to systematically compare the performance of models with and without CYGNSS data fusion. Specifically, CV was used solely for hyperparameter tuning and to demonstrate the overall performance on the training set, while the independent test set was reserved for the final evaluation. Furthermore, we examined the fusion methods under diverse experimental conditions, including varying durations of training data (3–27 months) and different data reconstruction approaches (*e.g.*, linear interpolation), to thoroughly validate the proposed method's robustness. For quantitative evaluation, three metrics were selected: the Pearson correlation coefficient (R), Nash-Sutcliffe efficiency (NSE), and root mean square error (RMSE) (Nash and Sutcliffe, 1970).

4. Results and analysis

4.1. Overall performance of the fused data model

To evaluate the general performance of the proposed method, we selected 15 hydrological stations distributed across different regions (data from January 1, 2021 to March 31, 2023) to show the temporal variation of estimated water levels (Fig. 7). To demonstrate the superiority of the method, comparative experimental results without CYGNSS data fusion were also presented. For a fair and direct comparison, both methods adopted 10-fold CV to randomly assess the overall model performance.

Fig. 7 shows the temporal variations of water level estimates at the 15 stations. The proposed fusion model, which incorporates CYGNSS data, performs well by aligning closely with observed measurements and significantly enhancing estimation accuracy and temporal resolution compared to the model without data fusion.

Table 3
Comparative evaluation of validation accuracy for data fusion with/without CYGNSS.

	Fusion with CYGNSS			Without CYGNSS		
	RMSE (m)	NSE	R	RMSE (m)	NSE	R
All stations	**0.1680**	**0.8764**	**0.9363**	**0.3411**	**0.7668**	**0.8765**
Baoyingbao	0.1160	0.6430	0.8249	0.2070	0.5230	0.7678
Chuandong Port	0.1153	0.4389	0.7176	0.1243	0.2194	0.6702
Dingnian	0.0952	0.2644	0.5784	0.1012	0.0251	0.2304
Fanchuan	0.1216	0.6601	0.8209	0.1242	0.4555	0.6830
Funing	0.0994	0.6081	0.7857	0.1170	0.2458	0.6223
Gaogang	0.1403	0.6381	0.8040	0.2348	0.1413	0.6752
Gaoyou	0.1805	0.8371	0.9168	0.3083	0.1501	0.6167
Huangqiao	0.1743	0.9491	0.9754	0.3274	0.7859	0.9126
Jiangdu	0.2456	0.7836	0.8865	0.3898	0.1608	0.5488
Mangdao	**0.2327**	**0.8731**	**0.9358**	**0.4706**	**0.1756**	**0.6402**
Sanduo	0.1070	0.6456	0.8162	0.2384	0.1278	0.4062
Sheyang Town	0.1192	0.6590	0.8433	0.1620	0.1159	0.6299
Taizhou	0.1382	0.1421	0.9952	0.1679	0.2029	0.4595
Xinghua	0.0938	0.6644	0.8241	0.1718	0.3114	0.6231
Yancheng	**0.0925**	**0.5888**	**0.7778**	**0.1149**	**0.3059**	**0.5847**

At Jiangdu Station, the fusion model effectively captures water level trends across different conditions, maintaining a strong correlation with observations, while the model without data fusion shows noticeable biases, especially during periods of change. At Mangdao Station, located near a sluice gate and heavily influenced by human activity, the fusion model excels in capturing real-time fluctuations, unlike the model without data fusion, which struggles with substantial errors. During the July 2021 flood event at Sanduo Station, the fusion model successfully detected an abnormal rise in water levels, demonstrating higher sensitivity and validation accuracy, whereas the model without data fusion failed to recognize this anomaly, resulting in significant prediction errors.

The quantitative evaluation results across all stations were shown in Table 3, providing a more precise and intuitive method for evaluating the results. For example, the Yancheng station demonstrated the best RMSE performance without CYGNSS (RMSE of 0.114 m). After data fusion, the RMSE decreased to 0.092 m, and the R value improved to 0.777. Furthermore, for stations where the initial error was larger and correlation was lower without data fusion, the improvement after data fusion was even more significant. For instance, due to the low-lying terrain, complex topography, and rapidly changing water flows, the estimation results for the Mangdao station were poorer compared to other stations under both conditions. This might be because greater environmental variability resulted in higher data noise, impacting the model's estimation capability. Nevertheless, after data fusion, the RMSE significantly decreased to 0.232 m (a 50 % reduction), and the R value reached 0.935 (an 46 % improvement).

Fig. 8 also features a scatter plot illustrating the data distribution. In the model incorporating data fusion, points in the scatter plot were more concentrated around the fitting line, highlighting a clear improvement in estimation accuracy. Conversely, the predictions from the model without data fusion appeared more dispersed. As demonstrated in Fig. 8a, the CV results show that the fusion of CYGNSS data significantly enhanced the model's performance. Across all stations, the RMSE was decreased from 0.341 m to 0.168 m, the NSE was improved from 0.766 to 0.876, and the correlation coefficient R was increased from 0.876 to 0.936, indicating a 50 % reduction in RMSE.

The improvement in water level estimation after data fusion can be attributed to several factors. First, the complementarity of diverse data sources allowed the model to utilize the physical characteristics of different data sources, compensating for the shortcomings of individual data sources. Second, data fusion reduced the impact of noise and errors

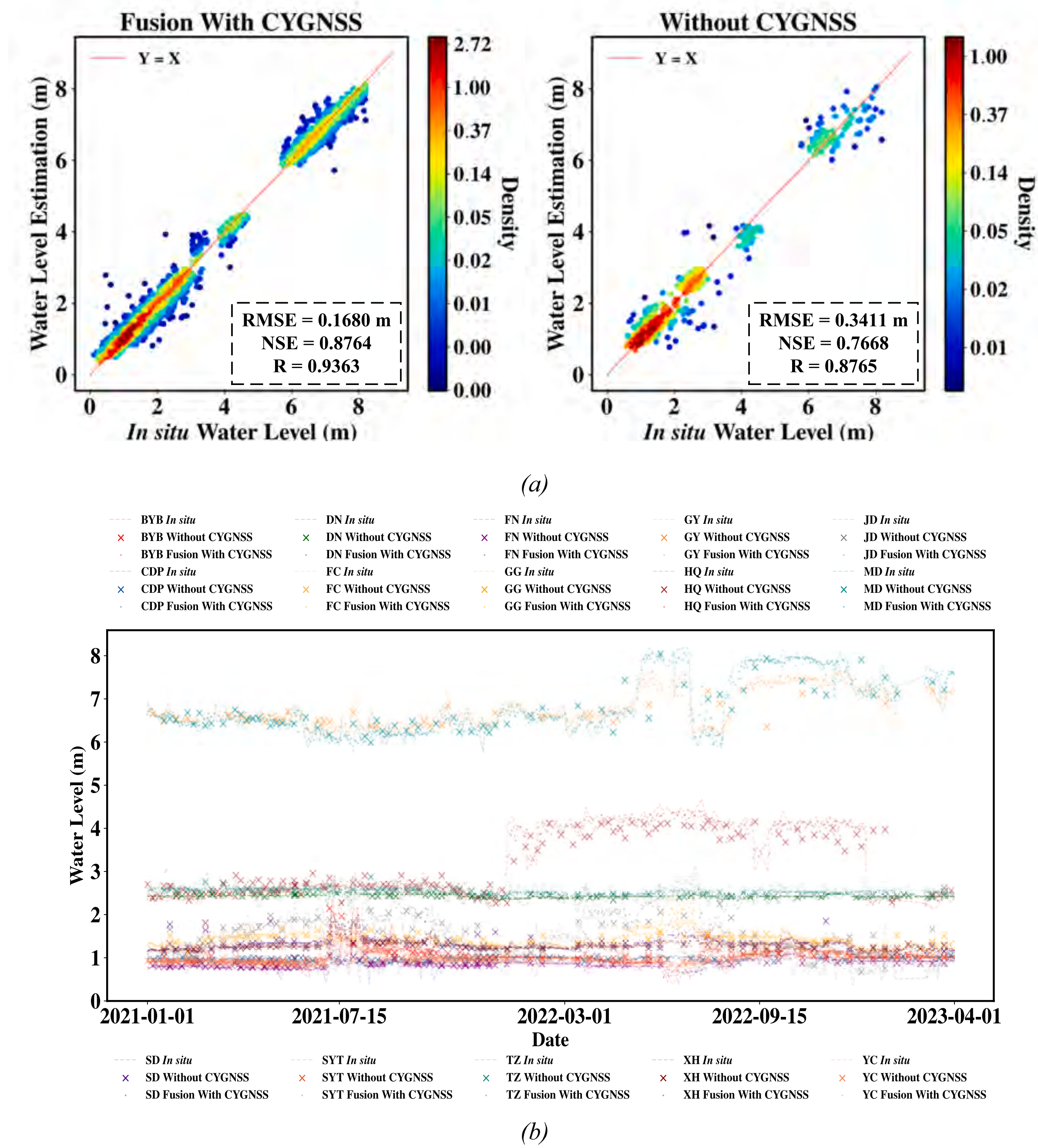

Fig. 8. Scatterplot analysis and temporal variations of water level estimation (fused with/without CYGNSS), (a) Scatterplot analysis, (b) Temporal variations of water level estimation.

from each data source on the model, thereby enhancing the accuracy of the estimations. Third, data fusion enhanced the model's robustness and feature extraction capabilities, improving its adaptability and fit across different environments. The fusion of Sentinel imagery and CYGNSS data significantly improved the estimation accuracy and resolution of water level estimation, providing reliable data for further research and practical applications.

4.2. Comparison with other ML methods for water level estimation

To further assess the water level estimation performance, we selected three different ML algorithms: RF, SVR, and XGBoost. All three algorithms used the same spatiotemporal fusion scheme and primary input features. The results were compared to identify the optimal ML modeling approach (Table 4).

In Table 4, the comparative evaluation of model performance metrics indicates that the XGBoost model performed the best overall, exhibiting high validation accuracy and stability. The RF model followed in validation accuracy, while the SVR model performed significantly worse, with lower NSE and *R* values indicating poorer estimation capabilities.

Due to the varying characteristics of station data, different estimation algorithms may perform optimally at different sites (see Fig. 9). The XGBoost approach consistently demonstrated the best result at various stations, with the highest NSE and *R* values along with the lowest RMSE values. Although the RF model demonstrated overall better validation accuracy than the SVR model, its performance was slightly lower than that of the SVR model at several stations. This suggests that the SVR model, while less effective on large datasets, can better capture local

Table 4
Evaluation metrics of river water level estimation performance based on data fusion at different stations.

	XGBoost			RF			SVR		
	RMSE (m)	NSE	R	RMSE (m)	NSE	R	RMSE (m)	NSE	R
All stations	**0.1680**	**0.8764**	**0.9363**	**0.1989**	**0.8407**	**0.9254**	**0.6279**	**0.7964**	**0.8970**
Baoying bao	0.1160	0.6430	0.8249	0.1310	0.5629	0.7652	0.1187	0.6193	0.8152
Chuandong Port	0.1153	0.4389	0.7176	0.1214	0.3814	0.6314	0.1601	0.0930	0.4646
Dingnian	0.0952	0.2644	0.5784	0.1069	0.2123	0.4974	0.1304	0.1008	0.3386
Fanchuan	0.1216	0.6601	0.8209	0.1413	0.5577	0.7603	0.1958	0.0843	0.6243
Funing	0.0994	0.6081	0.7857	0.1174	0.4561	0.6902	0.1215	0.4077	0.6509
Gaogang	0.1403	0.6381	0.8040	0.1692	0.4873	0.7266	0.1637	0.4684	0.7306
Gaoyou	0.1805	0.8371	0.9168	0.2406	0.7112	0.8548	0.2308	0.7350	0.8651
Huangqiao	0.1743	0.9491	0.9754	0.2614	0.8897	0.9540	0.2035	0.9314	0.9667
Jiangdu	0.2456	0.7836	0.8865	0.2822	0.7177	0.8605	0.3366	0.5789	0.8028
Mangdao	0.2327	0.8731	0.9358	0.3085	0.7767	0.8874	0.2456	0.8511	0.9257
Sanduo	0.1070	0.6456	0.8162	0.1192	0.5651	0.7678	0.1288	0.3980	0.7306
Sheyang Town	0.1192	0.6590	0.8433	0.1307	0.6089	0.7994	0.1214	0.6154	0.8327
Taizhou	0.1382	0.1421	0.9952	0.1419	0.1277	0.3802	0.1486	0.1051	0.3654
Xinghua	0.0938	0.6644	0.8241	0.1167	0.4964	0.7218	0.1097	0.4830	0.7725
Yancheng	0.0925	0.5888	0.7778	0.1029	0.5196	0.7294	0.1016	0.5093	0.7324

data variations when dealing with single-station data due to its suitability for small datasets and its reliance on kernel functions and parameter selection for handling nonlinear problems. In contrast, the XGBoost and RF models can manage complex nonlinear relationships more effectively and exhibit strong robustness and generalization ability, which allows them to outperform SVR models in many scenarios.

The most stable and robust results across various stations were achieved by the XGBoost model. As shown in Table 4 and Fig. 9, even at the Jiangdu station, which frequently experienced flooding and generally had poor estimation results, the XGBoost model still produced acceptable results, outperforming other algorithms. Compared to the RF model, the RMSE decreased by 0.036 m, and the R value increased by 0.026. All algorithms performed well at the Yancheng station. The reason may be that minimal water level changes reduce the impact of noise on the model, making the learning task relatively simple. This allowed the model to more easily capture the simple relationship between features and output during the training process, providing favorable conditions for water level predictions.

Thus, it can be concluded that the model's efficacy to generalize is governed by the characteristics of the observation stations, allowing for model selection or parameter optimization specific to different stations. Additionally, distinct models demonstrate unique strengths across various evaluation metrics. When estimating water levels in different regions, selecting the optimal model based on specific requirements can enhance the precision and dependability of the estimation results.

4.3. Independent testing results at different spatial and temporal scales

In addition to the presented 10-fold CV results for overall performance, it is important to assess the performance of the proposed method under spatially and temporally independent scenarios. The validation was exhibited across various spatial and temporal dimensions to thoroughly assess the XGBoost-based fusion model's performance. Apart from the commonly used 10-fold CV achieved by randomizing all samples (from 2021 to 01-01 to 2023-03-31), additional independent sites across different time periods (from 2023 to 04-01 to 2023-10-31) were shown to test model's robustness and generalization ability.

Eight stations of temporal variations comparisons in different locations were shown to demonstrate the robustness and generalization performance of the fused models. The clear consistency between the *in situ* measurements and the estimated water levels confirms the effectiveness of the proposed XGBoost-based fusion model. Without CYGNSS data fusion, the model fails to provide continuous daily water level estimations and exhibits notably lower estimation accuracy.

In the flood season of July 2023 (Fig. 10), we observed abrupt water level fluctuations at the Banjing, Dongtai, Yiling, and Zhongbao stations. The XGBoost-based fusion model effectively captured these abnormal fluctuations, but the model without data fusion was unable to address these significant extreme water level changes. Furthermore, at the Baoying, Jinghe, Jianhu, and Doulong Port stations, although there were frequent fluctuations in the observed water levels, the fusion model maintained robust estimation capabilities. By effectively capturing sustained and diverse water level fluctuations, it further validates its effectiveness in improving estimation accuracy and optimizing performance.

In the case of test samples, it is evident that the model without CYGNSS data fusion fails to accurately predict daily water levels and struggles to capture abrupt water level fluctuations. In contrast, the XGBoost-based fusion approach not only provides reliable daily water level observations but also significantly improves estimation accuracy and effectively monitors abrupt water level fluctuations, thereby demonstrating its superiority.

The test accuracy evaluation results, as detailed in Table 5, indicate that the XGBoost-based fusion model achieves an RMSE of 0.202 m, an NSE of 0.858, and an R of 0.927. These metrics demonstrate the model's strong performance in spatiotemporal water level estimation and its capability to predict water levels in regions without training samples. Compared to the sample-based 10-fold CV results (RMSE = 0.168 m, NSE = 0.876, R = 0.936), the fusion model shows slightly lower performance but still maintains high test accuracy, which is comparable and expected. This suggests that the proposed approach has good spatial generalization and robustness, making it a promising tool for water level estimation tasks under various regional and temporal conditions. In contrast, the model without CYGNSS fusion performs slightly worse at independent test sites, indicating weaker generalization capability and more difficulty adapting to new spatial or temporal domains.

Fig. 11 presents scatter plots of water level estimates from the XGBoost-based model on an independent test set. In Fig. 11a, the estimated values and the observed values are highly clustered along the fitted line, showing a distinct high-density linear band distribution. This indicates that the fusion model maintains a good fitting trend even at independent sites. However, in Fig. 11b, the scatter points demonstrate noticeable separation and clustering, deviating from the ideal fitted line with significant systematic biases, particularly underestimating at higher water levels. This suggests a reduced capacity of the model without CYGNSS fusion to adapt to spatiotemporal data.

4.4. Validation under different proportions of data modeling

In this section, we evaluate the changes in the model's estimation

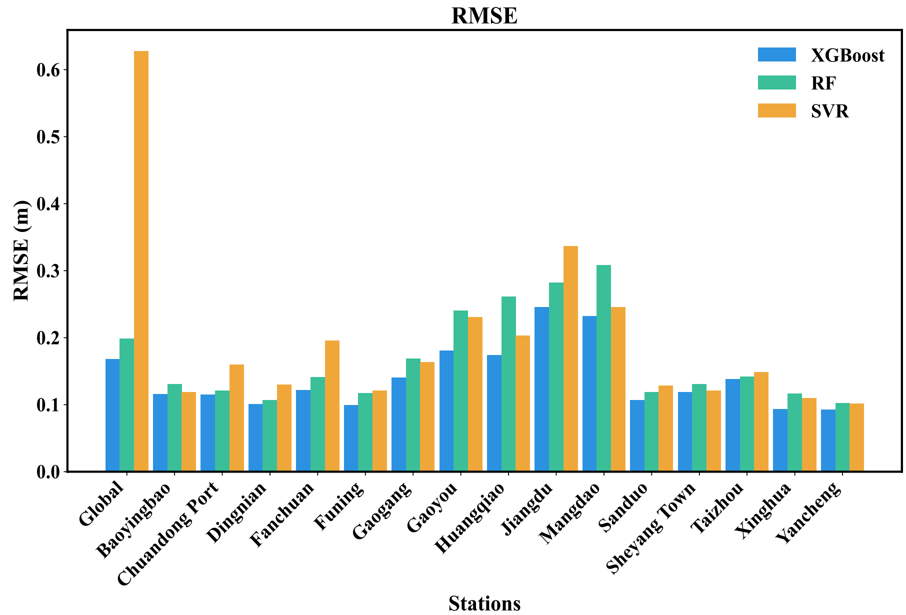

(a) *Root mean square error*

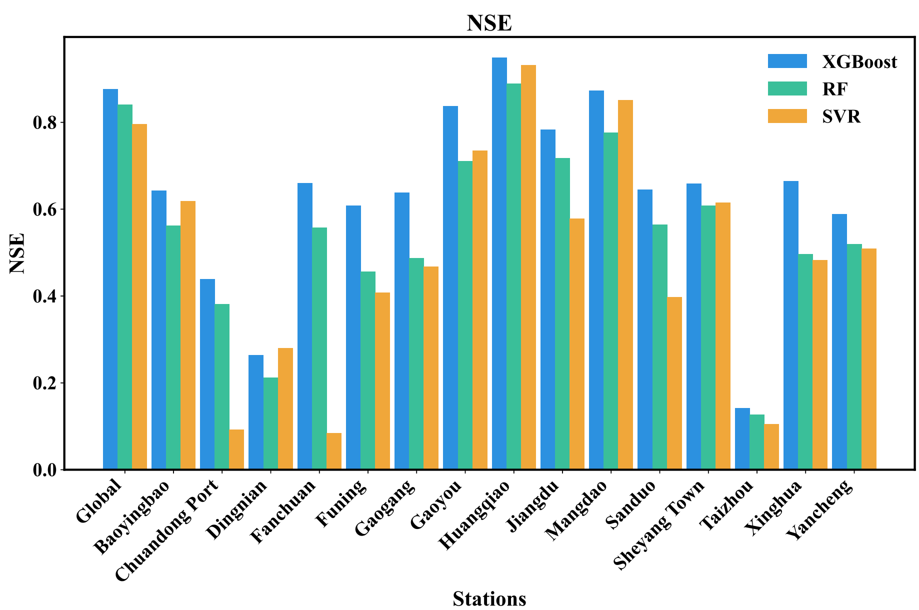

(b) *Nash–Sutcliffe efficiency*

Fig. 9. Distribution of validation accuracy and correlation coefficients, (a) Root mean square error, (b) Nash–Sutcliffe efficiency and (c) Pearson correlation coefficient.

performance by adjusting the length of the training data under different proportions of modeling data. In Fig. 12, we analyze the trends in water level estimates at test set from both the XGBoost-based fusion model and the model without CYGNSS fusion as the training period extends (varying time lengths). Fig. 13 presents the corresponding overall test accuracy metrics, including RMSE, NSE, and the correlation coefficient *R*.

It can be observed that as the training data extends from 3 months to 27 months, the model exhibits noticeable stage-wise changes in estimation performance. During the short-term data phase (3–12 months), the model finds it challenging to capture comprehensive water level variation patterns, such as seasonal and interannual changes, due to insufficient data. This results in high and fluctuating RMSE, with all three evaluation metrics performing poorly. As the modeling progresses to the mid-term data phase (12–21 months), the model's performance improves significantly with the data covering a complete hydrological cycle. RMSE gradually decreases and stabilizes, indicating that the model is increasingly capable of capturing the main patterns of water level changes. For long-term data (21–27 months), the model performance improvements enter a plateau, with the RMSE essentially converging, and further increases in data offering limited enhancements in test accuracy.

The overall performance trends of both the fused and without fusion models are largely consistent. During the initial stages, when data is

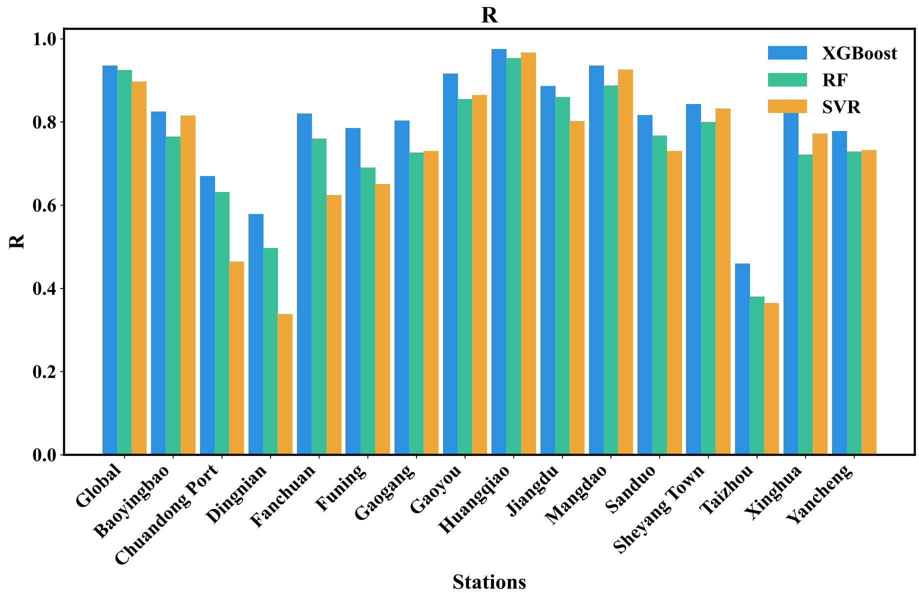

(c) *Pearson correlation coefficient*

Fig. 9. (*continued*).

limited, the estimation capabilities of both models are constrained, but as data accumulates, their generalization performance improves. Once the modeling duration reaches 15 months, the performance of both models stabilizes, suggesting that the data volume is adequate to support effective learning of the underlying patterns. Notably, the XGBoost-based fusion model consistently outperforms the model without CYGNSS across all modeling periods, with this advantage being particularly pronounced during periods of limited data (3–12 months). This finding indicates that CYGNSS data provides crucial supplementary hydrological information during the early stages of modeling, effectively enhancing the model's ability to detect water level variation patterns and mitigating the decline in model performance caused by insufficient training samples.

4.5. *Daily water level estimation of Sheyang River using the proposed scheme*

The daily river water level estimation model combining the XGBoost algorithm with fused Sentinel-1 imagery and CYGNSS data exhibited strong performance and stability across various datasets, demonstrating its reliability under different geographical and climatic conditions. The estimation results indicated high accuracy and practicality. Therefore, we applied this model to a specific case study, the Sheyang River, to further test its effectiveness in diverse scenarios. This case study aimed to validate the model's estimation accuracy and offer valuable insights and data support for future large-scale applications. Detailed monitoring results for the Sheyang River from June 1st to July 31st are displayed in Fig. 14.

The Sheyang River is an important outlet channel in the Lixiahe region, serving as a key part of the water cycle between the land and sea. The river water flows from inland areas and ultimately discharges into the Yellow Sea. Analysis of slope maps and digital elevation model (DEM) maps indicated that the Sheyang River generally flows from west to east. In Fig. 14b - Fig. 14d, the water level estimation results showed that the water levels on the west side were higher than those on the east side, with a dense distribution of estimation points indicating the river's flow direction. This indirectly confirmed the river's flow direction, preliminarily verifying the objectivity and accuracy of the proposed data model.

Water level data from *in situ* measurements were recorded simultaneously at the upstream Sheyang Town station and the downstream Sheyang River station (see Fig. 14e). On June 1, 2023, the upstream station recorded a water level of 1.08 m, while the downstream station recorded 1.37 m. The data from these two hydrological stations incorrectly indicated that the river flows from east to west. However, the middle section of the Sheyang River contains several significant meanders, creating complex hydrodynamic conditions. This complexity highlights the limitations of relying solely on data from a few specific points.

By June 13, the *in situ* water levels at the upstream and downstream stations were 0.87 m and 1.21 m, respectively. Although overall water levels had risen since June 1, the increase was consistent upstream and downstream, indicating stable flow within the observed river section during this period. The predicted water level showed minimal deviation from actual levels (within 0.01 m), demonstrating the model's excellent performance under stable conditions. Compared to *in situ* monitoring, the high-resolution characteristics of the estimation model captured subtle water level fluctuations more precisely.

In mid-July 2023, the Lixiahe region experienced several days of heavy rainfall. By July 31, the measured upstream and downstream water levels of the Sheyang River were 1.24 m and 0.91 m, respectively. The significant increase upstream, combined with a decrease downstream, led to an unusual situation where the upstream level was suddenly higher than the downstream level. The estimated water levels on July 31 confirmed the *in situ* water level changes, further validating the precision and effectiveness of the proposed model.

It can be concluded that during the heavy rainfall event, rainwater accumulated upstream, as evidenced by the measured and estimated water level changes. The low-lying terrain in the western upstream area ("pot bottom" terrain) impeded the smooth flow of rainwater downstream, leading to water accumulation upstream. Therefore, enhancing drainage measures through artificial intervention in specific areas is crucial for preventing potential flood disasters. This case study confirms the importance of continuous and accurate monitoring of regional hydrological changes for flood prevention and demonstrates the capability of the proposed model to accurately capture water level changes over a wide spatial range, providing new means and methods for monitoring river stability.

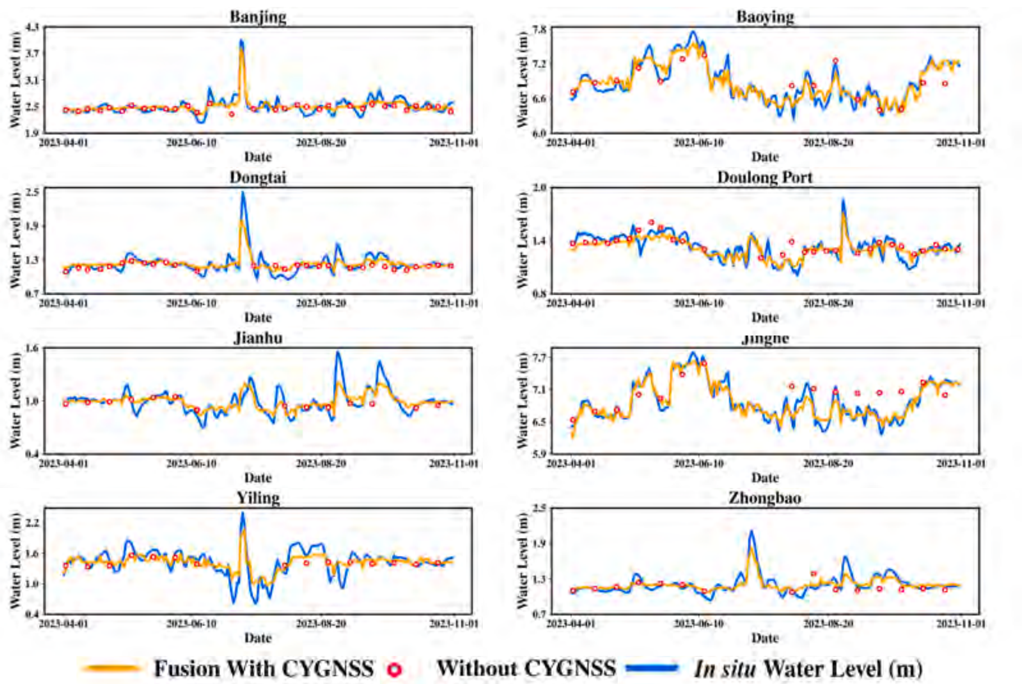

(a)

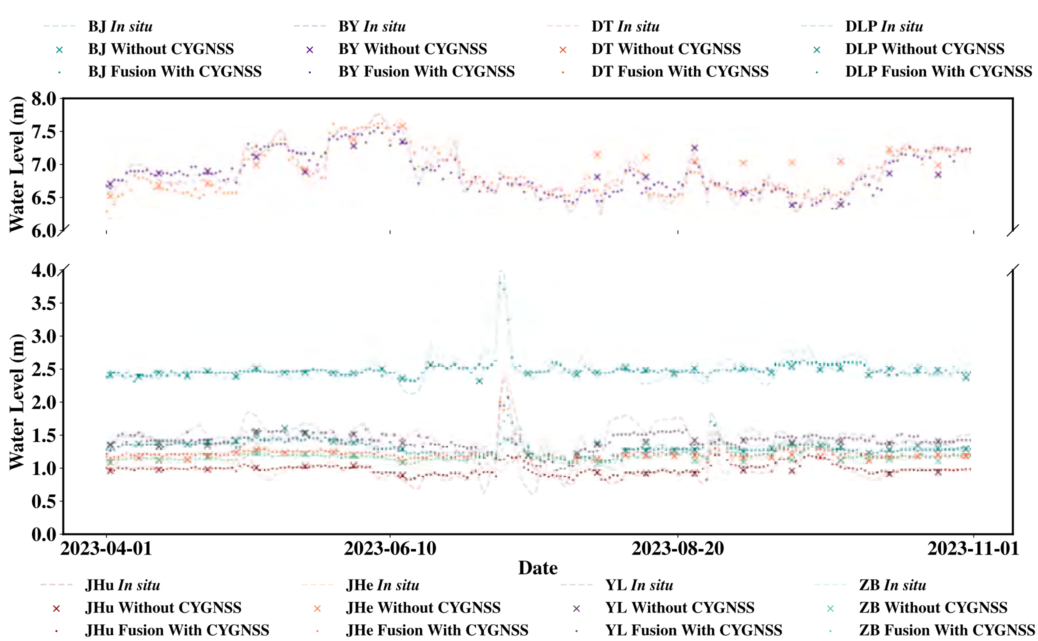

(b)

Fig. 10. Temporal variations comparison of water level estimation based on spatiotemporally independent station (fused with/without CYGNSS), (a) Test results for individual independent stations, (b) Aggregated results across all independent stations.

5. Discussion

5.1. Advantages and prospectives

This study successfully achieved high spatiotemporal resolution water level estimates by integrating CYGNSS data and Sentinel-1 imagery, significantly improving the accuracy and real-time performance of river water level monitoring. The high-frequency observation capability of CYGNSS makes it particularly suitable for capturing rapidly changing hydrological processes. The high spatial resolution of Sentinel-1 data provides detailed surface information, which helps to accurately identify water level changes and related geographic features. The effective integration of active and passive technologies not only ensures high spatial precision but also provides more frequent temporal data, thus offering crucial support for flood control and water resource management.

Table 5
Comparative evaluation of test accuracy for data fusion with/without CYGNSS.

	Fusion with CYGNSS			Without CYGNSS		
	RMSE (m)	NSE	R	RMSE (m)	NSE	R
All Stations	**0.2026**	**0.8589**	**0.9274**	**0.4799**	**0.7178**	**0.8488**
Banjing	0.1001	0.7549	0.8830	0.1264	0.1536	0.4198
Baoying	0.1194	0.8732	0.9360	0.1741	0.7511	0.8736
Dongtai	0.1026	0.6851	0.8856	0.0873	0.2490	0.5204
Doulong Port	0.0820	0.6157	0.8085	0.0881	0.3906	0.6582
Jianhu	0.0808	0.6209	0.8203	0.0518	0.4819	0.7202
Jinghe	0.1101	0.9052	0.9526	0.3218	0.3166	0.6683
Yiling	0.1565	0.6302	0.8421	0.1231	0.4105	0.7750
Zhongbao	0.0833	0.7364	0.9111	0.1176	0.1433	0.4363

This study was based on the practical needs of flood and drought management. Through extensive collaboration and long-term in-depth exploration, we employed advanced scientific methods, reflecting a problem-driven research approach. Our proposed SAR and CYGNSS data fusion model could be applied to an integrated information platform for flood control and drought prevention, contributing significantly to water resource allocation, management, and scheduling. The model can be used to monitor water level changes in real-time, providing rapid and accurate data and predictions, optimizing resource allocation, enhancing early warning capabilities, and reducing disaster losses. This not only promotes the development of smart water management but also provides robust data support for water engineering construction and management, especially in regions with scarce hydrological data, showcasing substantial application potential.

Furthermore, the results of this study are also applicable to multiple fields such as agricultural monitoring, environmental monitoring, urban planning, and management. In the future, through technological integration and innovation, fusion models are expected to achieve broader interdisciplinary applications, such as precision agriculture decision support, wetland ecosystem protection, urban expansion monitoring, and disaster risk assessment, further driving intelligent and refined management in various sectors and enhancing society's ability to efficiently utilize natural resources and protect the environment.

5.2. Effects of suitable algorithms and methods selection

5.2.1. Alternative algorithms for river width extraction

River width is a hydromorphological metric defined as the lateral distance between the water edges on either side of the river surface, measured perpendicular to the river's flow direction (Pavelsky and Smith, 2008). In this study, the RivWidthCloud algorithm (Yang et al., 2020) was used to extract river widths. This algorithm, based on the GEE platform, creates a water mask and measures widths along the river centerline, enabling rapid and efficient river width calculation. RivWidthCloud significantly enhances processing efficiency and reduces the need for manual intervention, making it particularly suitable for large watersheds with clearly defined river morphology. Its performance is especially notable when processing large-scale remote sensing datasets (Scherelis et al., 2023).

Despite its advantages in automated river width extraction, the algorithm has certain limitations. First, its accuracy depends heavily on the precision of water mask generation. Low-resolution RS imagery or inaccuracies in water extraction methods can lead to missing or erroneous water masks, affecting the accuracy of river width calculations. Second, the algorithm was originally designed for relatively wide rivers, and its performance is suboptimal for narrow or morphologically complex rivers (Yang et al., 2020). In such cases, it may fail to accurately identify river boundaries, resulting in inaccurate width measurements. Additionally, the presence of bridges and dams poses challenges. Real-world rivers often include artificial structures like bridges or dams, which can disrupt the water mask, causing abnormal segmentation and disconnected river skeletons, leading to inaccurate river width calculations.

Nevertheless, RivWidthCloud remains a mainstream solution for river width extraction due to its cost-effective, efficient, and automated characteristics. Future research could focus on optimizing the algorithm to improve its applicability and accuracy. For example, enhancing water mask extraction methods to minimize noise and errors or incorporating higher-resolution remote sensing data could significantly improve performance in complex terrains. Additionally, integrating advanced image processing techniques may further enhance the accuracy of river width extraction (Verma et al., 2021; Li et al., 2024; Xue et al., 2022).

5.2.2. ML-based spatiotemporal fusion methods

Spatiotemporal fusion approaches aim to predict fine-resolution data by integrating both time series and neighborhood information from at least two satellite sensors. Current data modeling methods can generally be classified into mathematical and learning-based approaches. Mathematical methods are typically based on mathematical models and algorithms, and they establish relationships between data by processing and analyzing small amounts of data. The advantage of these methods is their high computational efficiency, which allows for relatively accurate fusion results even with small datasets (Zhu et al., 2010; Emelyanova et al., 2013). However, when dealing with large datasets, it can lead to the construction of overly complex mathematical models, thereby limiting the flexibility of the model. Therefore, ML methods are proposed to address this issue and leverage the strengths of data integration (Zhao et al., 2020; Wang et al., 2024).

ML methods are entirely data-driven techniques that can automatically uncover complex relationships between different data sources by learning patterns and features from large datasets. When sufficient data

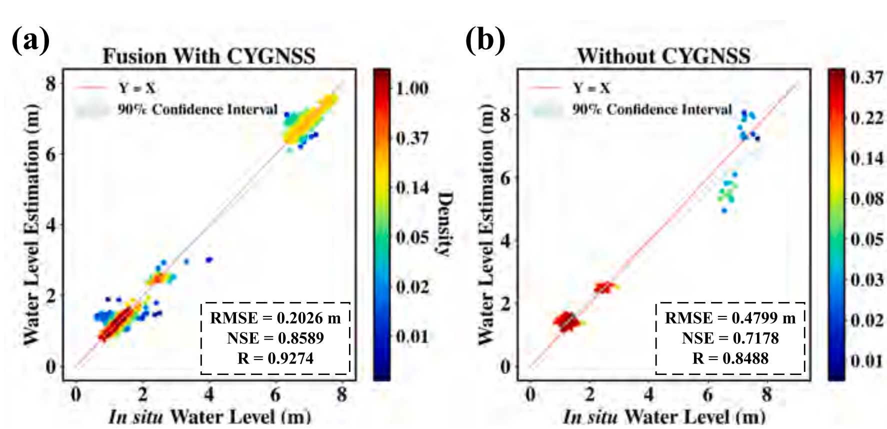

Fig. 11. Scatterplot analysis of water level estimation based on spatiotemporally independent stations, (a) fused with CYGNSS, (b) without CYGNSS.

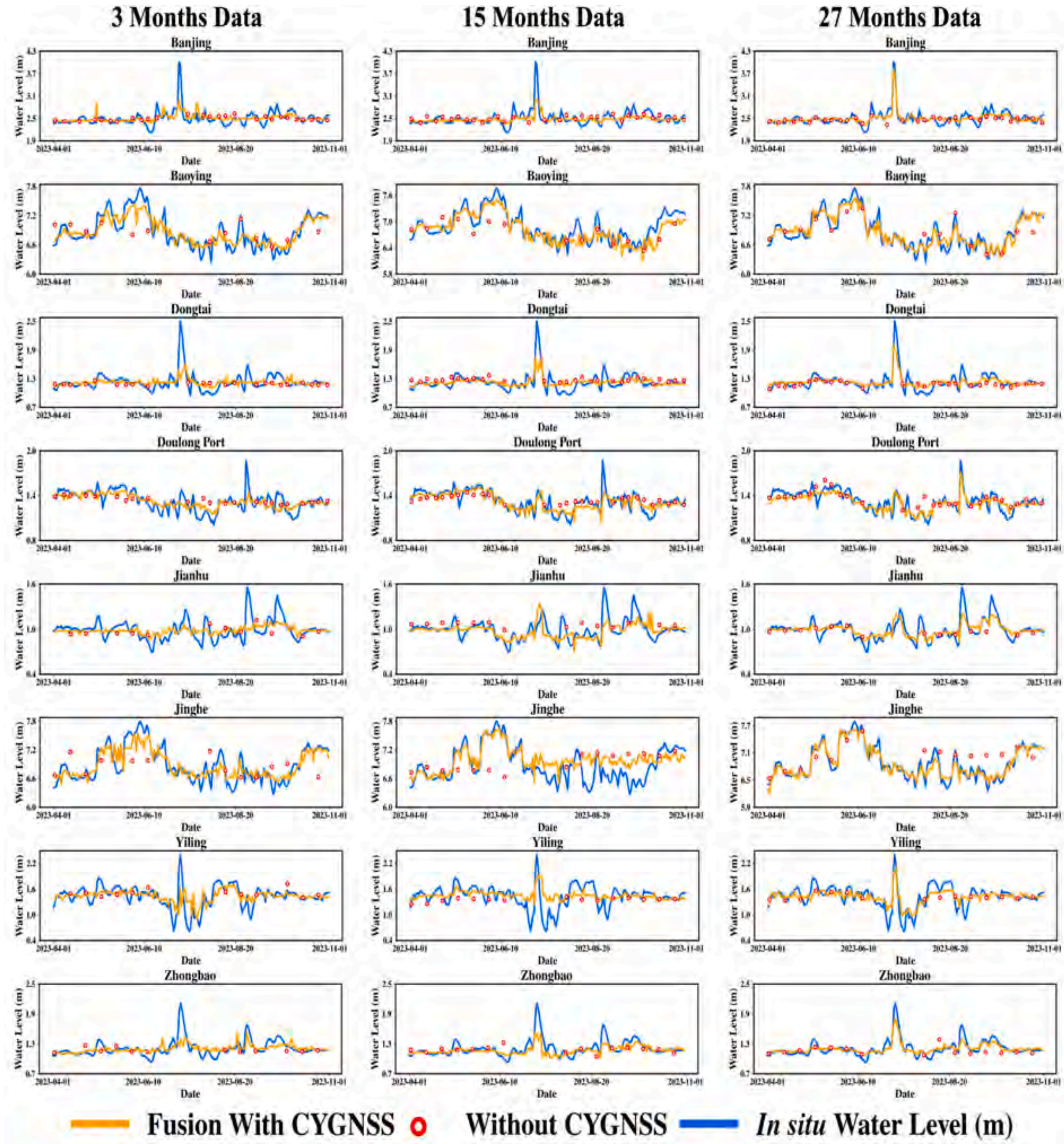

Fig. 12. Temporal variations comparison of water level predictions at spatiotemporally independent stations using models fused with and without CYGNSS data under different training data lengths (3, 15, and 27 months).

is available, ML can significantly enhance model accuracy and generalization ability, making it especially suitable for complex and nonlinear tasks. This study employed several popular ML algorithms to build fusion and water level estimation models. These algorithms have different architectures, resulting in variations in accuracy and efficiency. Tree-based ensemble algorithms generally outperform other ML algorithms, but their performance varies depending on data characteristics and parameter tuning (Kang et al., 2021; Xiao et al., 2017; Papadopoulos et al., 2018).

Unlike traditional ML methods, deep learning (DL), an important branch of ML, primarily uses multi-layer neural networks (such as convolutional neural networks and recurrent neural networks) for data learning and processing (LeCun et al., 2015). DL automatically extracts features from data without the need for manual feature selection, making it particularly effective in handling high-dimensional, nonlinear, and complex data (such as image and time series data). As a result, DL often exhibits stronger learning capabilities and higher prediction accuracy. However, the high computational demands and longer training times of ML may impact real-time applications and processing efficiency (Philippus et al., 2024). Future research could explore diverse AI modeling approaches, focusing on the dynamic features of time series data, and apply DL algorithms, like long short-term memory (LSTM) networks to capture temporal dependencies (Shi et al., 2015), to more accurately characterize hydrological processes and improve model performance while ensuring processing efficiency.

5.3. Limitation of CYGNSS data

Due to the continual movement of the eight CYGNSS satellites and the thirty-two Global Positioning System (GPS) satellites that act as the

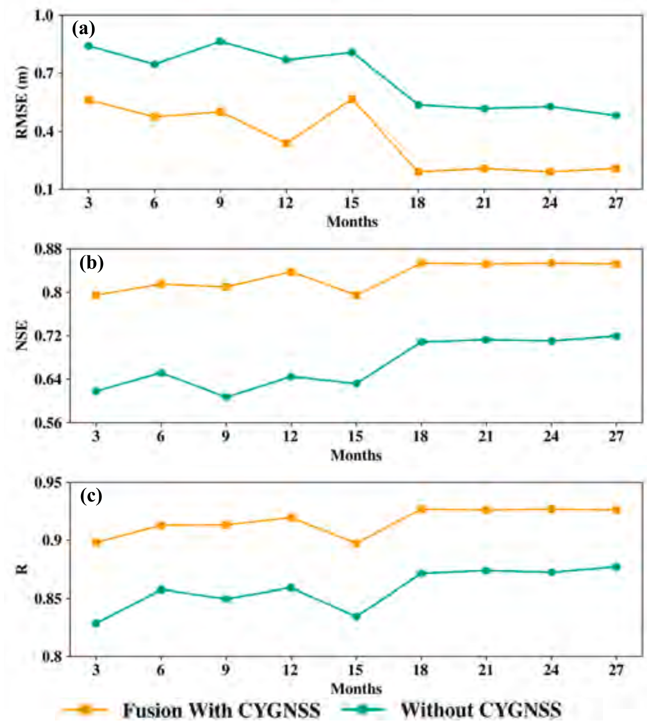

Fig. 13. Accuracy variation of water level predictions at independent validation stations under different proportions of training data. (a) Root mean square error, (b) Nash–Sutcliffe efficiency and (c) Pearson correlation coefficient.

transmitters, the point of reflection on the Earth's surface is constantly changing, which means that the surface is sampled pseudo-randomly. The CYGNSS satellites are each able to record up to four independent reflections at one time, and the mean repeat time is ~4 h (Ruf et al., 2012). Although the eight CYGNSS satellites sample both the ocean and land surface at all hours of the day, the quasi-randomly distributed nature of CYGNSS sampling, as well as the limited number of satellites (or insufficient receive channels on each instrument), leads to data gaps in daily observations (Chew and Small, 2020; Chew et al., 2023; Lei et al., 2022; Nguyen et al., 2025; Zeiger et al., 2022; Downs et al., 2023; Ma et al., 2024; Bu and Yu, 2022; Yueh et al., 2022; Zhang et al., 2022; Wei et al., 2024).

In contrast to typical remote sensing techniques that have repeatable swaths and the same local acquisition time, CYGNSS observables generally need to be transformed (using a time window) daily or monthly in consistent with other remote sensing and modeling data (Chew et al., 2023; Lei et al., 2022; Zeiger et al., 2022; Ma et al., 2024; Yueh et al., 2022; Zhang et al., 2022; Llamas et al., 2020). The filling of data gaps in this process led to enhanced data completeness and improved model robustness. This study employs a commonly used three-day sliding window and the Kriging interpolation method to address this well-known problem, this process may introduce some acceptable errors into the reflectivity used in this study and all other related works (Chew and Small, 2020; Lei et al., 2022; Zeiger et al., 2022; Ma et al., 2024; Yueh et al., 2022; Zhang et al., 2022; Wei et al., 2024; Chew and Small, 2018; Kim and Lakshmi, 2018; Al-Khaldi et al., 2019; Clarizia et al., 2019; Calabia et al., 2020; Yan et al., 2020; Jia et al., 2021).

Limited by the working mechanisms of CYGNSS satellites, their observational strategy focuses on tropical and subtropical regions (38°N to 38°S) where cyclonic activity is prevalent, making full global spatial coverage currently unattainable. Nevertheless, the methods and results we propose perform exceptionally well within the covered region, holding significant scientific and practical value, while also providing important insights for future improvements. In the future, increasing the number of GNSS-R satellites, developing GNSS-R receivers capable of recording more than four reflections simultaneously (technologies already in development), and expanding data sampling coverage (*e.g.*, missions such as HydroGNSS (Unwin et al., 2021) and CYGNSS-FOLLOWON (Norris et al., 2018; Moller et al., 2021)) will be key to addressing this issue. With greater data availability, the applicability of this method will be further enhanced. We look forward to further validating and refining these methods in future studies to address broader geographical ranges and application scenarios.

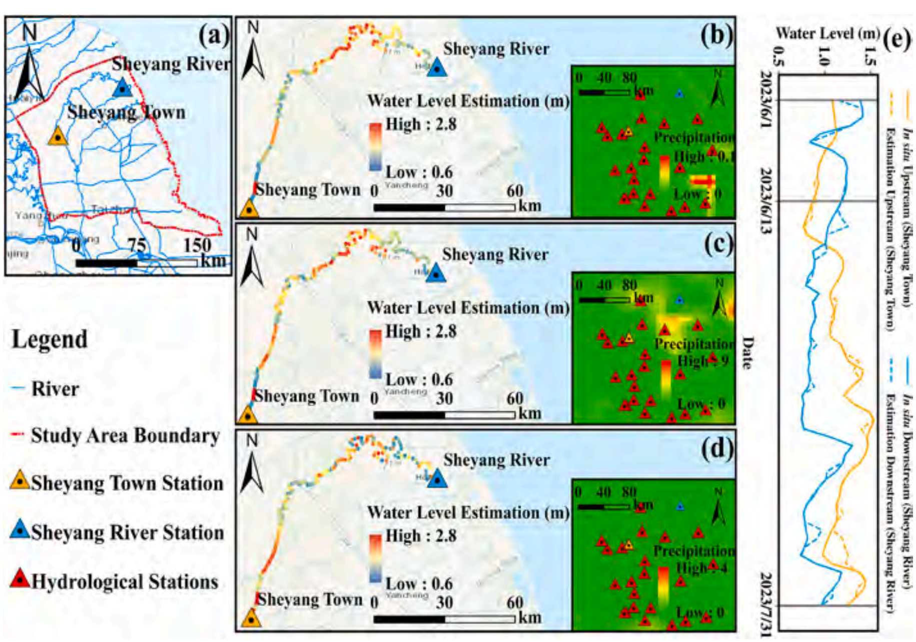

Fig. 14. Water levels estimation of Sheyang River and precipitation distribution in the Lixiahe region, (a) Locations of upstream and downstream hydrological stations, (b-d) Predicted continuous water level distribution on June 1, June 13, and July 31, (e) Upstream and downstream temporal variations in water level estimation compared to *in situ* measurements.

6. Conclusion

In this study, we developed an innovative model for estimating daily water levels using fused data and ML methods. This model leverages the benefits of CYGNSS and Sentinel-1 SAR data, combined with the XGBoost algorithm, using the fused high-resolution temporal-spatial inputs such as CYGNSS-derived reflectivity, Sentinel-1 SAR-derived backscattering coefficient (VV and VH), and river width. Comprehensive experiments were conducted using various ML algorithms and feature optimization to validate the proposed method's effectiveness. The effectiveness of the model was evaluated based on over 15 uniformly distributed gauge stations in the Lixiahe region. The 10-fold CV method was employed, with additional validation conducted across different spatial and temporal scales to ensure independence between the training and test datasets.

Water level estimation was improved significantly after data fusion, as evidenced by enhanced RMSE, Nash-Sutcliffe efficiency, and Pearson correlation coefficient. The fused data with the XGBoost algorithm provided the highest estimation accuracy, achieving the lowest RMSE (0.168 m), the highest NSE value (0.876) and the highest R value (0.936). Specifically, integrating Sentinel-1 imagery and CYGNSS data significantly enhanced river water level estimation and showed a notable 50.74 % increase in validation accuracy. To further evaluate the model's generalizability, we conducted testing on eight spatially and temporally independent hydrological stations. Results showed that the fusion method reduced RMSE from 0.479 to 0.202 and increased R from 0.848 to 0.927. These findings confirm that this data fusion approach enhanced the model's temporal resolution and estimation accuracy, demonstrating substantial improvements regardless of the specific algorithm or data amount used.

The complementarity of CYGNSS and Sentinel-1 SAR data allowed the model to utilize the benefits derived from high temporal and spatial data variation characteristics, offsetting the limitations of single data sources. Importantly, our proposed method, using backscattering coefficients as the main feature variable, effectively captured and reflected river water level fluctuations through Sentinel-1 SAR and CYGNSS fusion data. Our fusion method demonstrates consistent effectiveness, which stems from its inherent mechanism rather than dependence on data density. This approach is not constrained by river morphology and is particularly suitable for artificial rivers with approximately vertical profiles, enabling accurate monitoring of changes in river water levels. Once validated, this methodology will eliminate the need for existing *in situ* measurement data, allowing for dynamic monitoring of river water levels with high spatiotemporal resolution.

CRediT authorship contribution statement

Yan Jia: Writing – review & editing, Methodology, Formal analysis, Conceptualization. **Quan Liu:** Writing – original draft, Visualization, Validation, Software, Data curation. **Chunqiao Song:** Writing – review & editing. **Zhiyu Xiao:** Visualization. **Qiang Dai:** Writing – review & editing. **Shuanggen Jin:** Supervision, Funding acquisition. **Patrizia Savi:** Validation, Supervision.

Declaration of competing interest

The authors declare that they have no known competing financial interests or personal relationships that could have appeared to influence the work reported in this paper.

Acknowledgment

Support for this work was provided by the National Key Research and Development Program of China (Grant No. 2022YFF0711603), Henan International Science and Technology Cooperation Key Program (Grant No. 241111520700), National Natural Science Foundation of China (Grant No. 42001375), and Postgraduate Research & Practice Innovation Program of Jiangsu Province (Grant No. KYCX25_1216). The authors express their gratitude to the SAR and CYGNSS teams, as well as the Flood and Drought Disaster Prevention and Dispatch Command Center of Jiangsu Province for providing the dataset used in this study.

Data availability

Data will be made available on request.

References

Al-Khaldi, M.M., Johnson, J.T., O'Brien, A.J., Balenzano, A., Mattia, F., 2019. Timeseries retrieval of soil moisture using CYGNSS. IEEE Trans. Geosci. Remote Sens. 57 (7), 4322–4331.

Alsdorf, D.E., Rodríguez, E., Lettenmaier, D.P., 2007. Measuring surface water from space. Rev. Geophys. 45 (2), Rg2002. https://doi.org/10.1029/2006rg000197.

Altenau, E.H., Pavelsky, T.M., Durand, M.T., Yang, X., Frasson, R.P.D., Bendezu, L., 2021. The surface water and ocean topography (SWOT) Mission River database (SWORD): A Global River network for satellite data products. Water Resour. Res. 57 (7). https://doi.org/10.1029/2021WR030054 e2021WR030054.

Bao, F., Wu, S., Gao, J., Yuan, S., Liu, Y., Huang, K., 2024. Continental aerosol properties and absorption retrieval using random forest machine learning method specific to geostationary remote sensing. Remote Sens. Environ. 311, 114275. https://doi.org/10.1016/j.rse.2024.114275.

Birkett, C.M., 1998. Contribution of the TOPEX NASA radar altimeter to the global monitoring of large rivers and wetlands. Water Resour. Res. 34 (5), 1223–1239. https://doi.org/10.1029/98wr00124.

Birkett, C.M., Mertes, L.A.K., Dunne, T., Costa, M.H., Jasinski, M.J., 2002. Surface water dynamics in the Amazon Basin: application of satellite radar altimetry. J. Geophys. Res.-Atmos. 107 (D20), 8059. https://doi.org/10.1029/2001jd000609.

Biswas, N.K., Hossain, F., Bonnema, M., Okeowo, M.A., Lee, H., 2019. An altimeter height extraction technique for dynamically changing rivers of south and South-East Asia. Remote Sens. Environ. 221, 24–37. https://doi.org/10.1016/j.rse.2018.10.033.

Bu, J., Yu, K., 2022. Sea surface rainfall detection and intensity retrieval based on GNSS-reflectometry data from the CYGNSS mission. IEEE Trans. Geosci. Remote Sens. 60, 1–15. https://doi.org/10.1109/TGRS.2021.3127943.

Calabia, A., Molina, I., Jin, S., 2020. Soil moisture content from GNSS reflectometry using dielectric permittivity from fresnel reflection coefficients. Remote Sens. 12 (1), 122.

Calmant, S., Seyler, F., Cretaux, J.F., 2008. Monitoring continental surface waters by satellite altimetry. Surv. Geophys. 29 (4–5), 247–269. https://doi.org/10.1007/s10712-008-9051-1.

Chen, F., Zhang, M., Zhao, H., Guan, W., Yang, A., 2024. Pakistan's 2022 floods: spatial distribution, causes and future trends from sentinel-1 SAR observations. Remote Sens. Environ. 304, 114055. https://doi.org/10.1016/j.rse.2024.114055.

Chew, C.C., Small, E.E., 2018. Soil moisture sensing using spaceborne GNSS reflections: comparison of CYGNSS reflectivity to SMAP soil moisture. Geophys. Res. Lett. 45 (9), 4049–4057.

Chew, C., Small, E., 2020. Estimating inundation extent using CYGNSS data: A conceptual modeling study. Remote Sens. Environ. 246, 111869. https://doi.org/10.1016/j.rse.2020.111869.

Chew, C., Small, E., Huelsing, H., 2023. Flooding and inundation maps using interpolated CYGNSS reflectivity observations. Remote Sens. Environ. 293, 113598. https://doi.org/10.1016/j.rse.2023.113598.

Clarizia, M.P., Ruf, C., Cipollini, P., Zuffada, C., 2016. First spaceborne observation of sea surface height using GPS-reflectometry. Geophys. Res. Lett. 43 (2), 767–774. https://doi.org/10.1002/2015gl066624.

Clarizia, M.P., Pierdicca, N., Costantini, F., Floury, N., 2019. Analysis of CYGNSS data for soil moisture retrieval. IEEE J. Sel. Top. Appl. Earth Obs. Remote Sens. 12 (7), 2227–2235.

Comite, D., Ticconi, F., Dente, L., Guerriero, L., Pierdicca, N., 2019. Bistatic coherent scattering from rough soils with application to GNSS reflectometry. IEEE Trans. Geosci. Remote Sens. 58 (1), 612–625. https://doi.org/10.1109/TGRS.2019.2938442.

Cooley, S.W., Ryan, J.C., Smith, L.C., 2021. Human alteration of global surface water storage variability. Nature 591 (7848), 78–81. https://doi.org/10.1038/s41586-021-03262-3.

Cordeiro, M.C.R., Martinez, J.M., Pena-Luque, S., 2021. Automatic water detection from multidimensional hierarchical clustering for Sentinel-2 images and a comparison with level 2A processors. Remote Sens. Environ. 253. https://doi.org/10.1016/j.rse.2020.112209.

Crétaux, J.-F., Arsen, A., Calmant, S., Kouraev, A., Vuglinski, V., Bergé-Nguyen, M., Gennero, M.-C., Nino, F., Del Rio, R.A., Cazenave, A., 2011. SOLS: A lake database to monitor in the near real time water level and storage variations from remote sensing data. Adv. Space Res. 47 (9), 1497–1507. https://doi.org/10.1016/j.asr.2011.01.004.

Dastour, H., Hassan, Q.K., 2023. A machine-learning framework for modeling and predicting monthly streamflow time series. Hydrology 10 (4), 95. https://doi.org/10.3390/hydrology10040095.

Dastour, H., Ghaderpour, E., Hassan, Q.K., 2022. A combined approach for monitoring monthly surface water/ice dynamics of Lesser Slave Lake via earth observation data. IEEE J. Sel. Top. Appl. Earth Obs. Remote Sens. 15, 6402–6417. https://doi.org/10.1109/Jstars.2022.3196611.

Downs, B., Kettner, A.J., Chapman, B.D., Brakenridge, G.R., O'Brien, A.J., Zuffada, C., 2023. Assessing the relative performance of GNSS-R flood extent observations: case study in South Sudan. IEEE Trans. Geosci. Remote Sens. 61, 1–13. https://doi.org/10.1109/TGRS.2023.3237461.

Durand, M., Fu, L.L., Lettenmaier, D.P., Alsdorf, D.E., Rodriguez, E., Esteban-Fernandez, D., 2010. The surface water and ocean topography Mission: observing terrestrial surface water and oceanic submesoscale eddies. Proc. IEEE 98 (5), 766–779. https://doi.org/10.1109/Jproc.2010.2043031.

Emelyanova, I.V., McVicar, T.R., Van Niel, T.G., Li, L.T., van Dijk, A.I.J.M., 2013. Assessing the accuracy of blending Landsat-MODIS surface reflectances in two landscapes with contrasting spatial and temporal dynamics: A framework for algorithm selection. Remote Sens. Environ. 133, 193–209. https://doi.org/10.1016/j.rse.2013.02.007.

Ferrentino, E., Nunziata, F., Buono, A., Urciuoli, A., Migliaccio, M., 2020. Multipolarization time series of Sentinel-1 SAR imagery to analyze variations of reservoirs' water body. IEEE J. Sel. Top. Appl. Earth Obs. Remote Sens. 13, 840–846. https://doi.org/10.1109/Jstars.2019.2961563.

Frappart, F., Seyler, F., Martinez, J., Leon, J., Cazenave, A., 2005. Determination of the water volume in the Negro River sub basin by combination of satellite and in situ data. Remote Sens. Environ. 99, 387–399. https://doi.org/10.1016/j.rse.2005.08.016.

Frappart, F., Papa, F., Famiglietti, J.S., Prigent, C., Rossow, W.B., Seyler, F., 2008. Interannual variations of river water storage from a multiple satellite approach: A case study for the Rio Negro River basin. J. Geophys. Res.-Atmos. 113 (D21), D21104. https://doi.org/10.1029/2007jd009438.

Fu, L.L., Alsdorf, D., Morrow, R., Rodriguez, E., Mognard, N., 2012. SWOT : The Surface Water and Ocean Topography Mission : Wide- Swath Altimetric Elevation on Earth. JPL Open Repository. https://hdl.handle.net/2014/41996.

Garg, S., Dasgupta, A., Motagh, M., Martinis, S., Selvakumaran, S., 2024. Unlocking the full potential of sentinel-1 for flood detection in arid regions. Remote Sens. Environ. 315, 114417. https://doi.org/10.1016/j.rse.2024.114417.

Garkoti, A., Kundapura, S., 2021. Deriving water level and discharge estimation using satellite altimetry for Krishna River. Karnataka. Remote Sensing Applications-Society and Environment 22, 100487. https://doi.org/10.1016/j.rsase.2021.100487.

Grimaldi, S., Xu, J., Li, Y., Pauwels, V.R.N., Walker, J.P., 2020. Flood mapping under vegetation using single SAR acquisitions. Remote Sens. Environ. 237, 111582. https://doi.org/10.1016/j.rse.2019.111582.

Guo, J.Y., Luan, Y.J., Li, Z., Liu, X., Li, C.M., Chang, X.T., 2021. Mozambique flood (2019) caused by tropical cyclone Idai monitored from Sentinel-1 and Sentinel-2 images. IEEE J. Sel. Top. Appl. Earth Obs. Remote Sens. 14, 8761–8772. https://doi.org/10.1109/Jstars.2021.3107279.

Hamunyela, E., Hipondoka, M., Persendt, F., Nghiyalwa, H.S., Thomas, C., Matengu, K., 2022. Spatio-temporal characterization of surface water dynamics with Landsat in endorheic Cuvelai-Etosha Basin (1990-2021). ISPRS J. Photogramm. Remote Sens. 191, 68–84. https://doi.org/10.1016/j.isprsjprs.2022.07.007.

Hostache, R., Matgen, P., Schumann, G., Puech, C., Hoffmann, L., Pfister, L., 2009. Water level estimation and reduction of hydraulic model calibration uncertainties using satellite SAR images of floods. IEEE Trans. Geosci. Remote Sens. 47 (2), 431–441. https://doi.org/10.1109/Tgrs.2008.2008718.

Hou, A.Y., Kakar, R.K., Neeck, S., Azarbarzin, A.A., Kummerow, C.D., Kojima, M., Oki, R., Nakamura, K., Iguchi, T., 2014. The global precipitation measurement Mission. Bull. Am. Meteorol. Soc. 95 (5), 701–702. https://doi.org/10.1175/Bams-D-13-00164.1.

Hu, Y.L., Zhou, Q., Li, T., Wang, H.S., Jiang, L.M., Shen, X., 2023. Accurate estimation of lake levels by the spatio-temporal modeling of satellite altimetry data. Remote Sens. Environ. 295, 113681. https://doi.org/10.1016/j.rse.2023.113681.

Huang, Q., Long, D., Du, M.D., Zeng, C., Li, X.D., Hou, A.Z., Hong, Y., 2018. An improved approach to monitoring Brahmaputra River water levels using retracked altimetry data. Remote Sens. Environ. 211, 112–128. https://doi.org/10.1016/j.rse.2018.04.018.

Iervolino, P., Guida, R., Iodice, A., Riccio, D., 2014. Flooding water depth estimation with high-resolution SAR. IEEE Trans. Geosci. Remote Sens. 53 (5), 2295–2307. https://doi.org/10.1109/TGRS.2014.2358501.

Jia, Y., Jin, S., Chen, H., Yan, Q., Savi, P., Jin, Y., Yuan, Y., 2021. Temporal-spatial soil moisture estimation from CYGNSS using machine learning regression with a preclassification approach. IEEE J. Sel. Top. Appl. Earth Observ. Remote Sens. 14, 4879–4893. https://doi.org/10.1109/JSTARS.2021.3076470.

Jia, Y., Xiao, Z.Y., Jin, S.G., Yan, Q.Y., Jin, Y., Li, W.M., Savi, P., 2024a. Improving CYGNSS-based soil moisture coverage through autocorrelation and machine learning-aided method. IEEE J. Sel. Top. Appl. Earth Obs. Remote Sens. 17, 12554–12566. https://doi.org/10.1109/Jstars.2024.3419779.

Jia, Y., Zou, J.Q., Jin, S.G., Yan, Q.Y., Chen, Y.X., Jin, Y., Savi, P., 2024b. Multiresolution soil moisture products based on a spatially adaptive estimation model and CYGNSS data. GISci. Remote Sens. 61 (1), 2313812. https://doi.org/10.1080/15481603.2024.2313812.

Jiang, H., Ji, L., Yu, K., Zhao, Y., 2024. Analysis of the substantial growth of water bodies during the urbanization process using landsat imagery—a case study of the lixiahe region. China. Remote Sens. 16, 711. https://doi.org/10.3390/rs16040711.

Jin, S.G., Camps, A., Jia, Y., Wang, F., Martin-Neira, M., Huang, F.X., Yan, Q.Y., Zhang, S.C., Li, Z.Y., Edokossi, K., Yang, D.K., Xiao, Z.Y., Ma, Z.M., Bai, W.H., 2024. Remote sensing and its applications using GNSS reflected signals: advances and prospects. Satell. Navig. 5 (1), 19. https://doi.org/10.1186/s43020-024-00139-4.

Jin, S.G., Chen, Z., Peng, H., 2025a. High-frequency water level estimation in the Yangtze River using multi-GNSS interferometric reflectometry. IEEE Trans. Geosci. Remote Sens. 63.

Jin, S.G., Wu, X., Qiu, H., 2025b. GNSS-Reflectometry: Fundamentals, Methods and Applications. Springer, Germany, pp. 1–326.

Kang, M.C., Yoo, D.Y., Gupta, R., 2021. Machine learning-based prediction for compressive and flexural strengths of steel fiber-reinforced concrete. Constr. Build. Mater. 266, 121117. https://doi.org/10.1016/j.conbuildmat.2020.121117.

Kim, H., Lakshmi, V., 2018. Use of cyclone global navigation satellite system (CYGNSS) observations for estimation of soil moisture. Geophys. Res. Lett. 45 (16), 8272–8282.

Kleinherenbrink, M., Naeije, M., Slobbe, C., Egido, A., Smith, W., 2020. The performance of CryoSat-2 fully-focussed SAR for inland water-level estimation. Remote Sens. Environ. 237, 111589. https://doi.org/10.1016/j.rse.2019.111589.

Koblinsky, C.J., Clarke, R.T., Brenner, A., Frey, H., 1993. Measurement of river level variations with satellite altimetry. Water Resour. Res. 29 (6), 1839–1848. https://doi.org/10.1029/93WR00542.

Kushwaha, A.P., Gupta, P.K., Pradhan, R., Pandey, A.C., 2022. Sensitivity analysis of C and Ku-band Scatterometers for river water level estimation. IEEE Trans. Geosci. Remote Sens. 60, 1–8. https://doi.org/10.1109/Tgrs.2022.3187173.

Larson, K.M., Löfgren, J.S., Haas, R., 2013. Coastal Sea level measurements using a single geodetic GPS receiver. Adv. Space Res. 51 (8), 1301–1310. https://doi.org/10.1016/j.asr.2012.04.017.

LeCun, Y., Bengio, Y., Hinton, G., 2015. Deep learning. Nature 521 (7553), 436–444. https://doi.org/10.1038/nature14539.

Lee, J.S., 1980. Digital image enhancement and noise filtering by use of local statistics. IEEE Trans. Pattern Anal. Mach. Intell. 2 (2), 165–168. https://doi.org/10.1109/tpami.1980.4766994.

Lei, F., Senyurek, V., Kurum, M., Gurbuz, A.C., Boyd, D., Moorhead, R., Crow, W.T., Eroglu, O., 2022. Quasi-global machine learning-based soil moisture estimates at high spatio-temporal scales using CYGNSS and SMAP observations. Remote Sens. Environ. 276, 113041. https://doi.org/10.1016/j.rse.2022.113041.

Li, W., Cardellach, E., Fabra, F., Ribó, S., Rius, A., 2019a. Assessment of spaceborne GNSS-R Ocean altimetry performance using CYGNSS mission raw data. IEEE Trans. Geosci. Remote Sens. 58 (1), 238–250. https://doi.org/10.1109/TGRS.2019.2936108.

Li, X.D., Long, D., Huang, Q., Han, P.F., Zhao, F.Y., Wada, Y., 2019b. High-temporal-resolution water level and storage change data sets for lakes on the Tibetan plateau during 2000-2017 using multiple altimetric missions and Landsat-derived lake shoreline positions. Earth Syst. Sci. Data. 11 (4), 1603–1627. https://doi.org/10.5194/essd-11-1603-2019.

Li, L.R., Su, H.J., Du, Q., Wu, T.X., 2021. A novel surface water index using local background information for long term and large-scale Landsat images. ISPRS J. Photogramm. Remote Sens. 172, 59–78. https://doi.org/10.1016/j.isprsjprs.2020.12.003.

Li, L., Elhajj, M., Feng, Y., Ochieng, W.Y., 2023a. Machine learning based GNSS signal classification and weighting scheme design in the built environment: a comparative experiment. Satellite Navigation 4 (1), 12.

Li, Z., Guo, F., Chen, F., Zhang, Z., Zhang, X., 2023b. Wind speed retrieval using GNSS-R technique with geographic partitioning. Satell Navig 4, 4. https://doi.org/10.1186/s43020-022-00093-z.

Li, H., Xu, Z., Zhou, Y., He, X., He, M., 2023c. Flood monitoring using sentinel-1 SAR for agricultural disaster assessment in poyang lake region. Remote Sens 15, 5247. https://doi.org/10.3390/rs15215247.

Li, M.M., Zhao, C.S., Duan, Z., Cheng, H.G., Lian, Y.Q., Wang, G.Q., 2024. Mechanically and accurately calculate river width in vegetation areas by coupling Sentinel-1 and-2 imageries within land-water-mixed pixels. J. Hydrol. 643, 131913. https://doi.org/10.1016/j.jhydrol.2024.131913.

Llamas, R.M., Guevara, M., Rorabaugh, D., Taufer, M., Vargas, R., 2020. Spatial gap-filling of ESA CCI satellite-derived soil moisture based on geostatistical techniques and multiple regression. Remote Sens. 12, 665. https://doi.org/10.3390/rs12040665.

Löfgren, J.S., Haas, R., Johansson, J.M., 2011. Monitoring coastal sea level using reflected GNSS signals. Adv. Space Res. 47 (2), 213–220. https://doi.org/10.1016/j.asr.2010.08.015.

Lowe, S.T., LaBrecque, J.L., Zuffada, C., Romans, L.J., Young, L.E., Hajj, G.A., 2002a. First spaceborne observation of an earth-reflected GPS signal. Radio Sci. 37 (1), 1–28. https://doi.org/10.1029/2000rs002539.

Lowe, S.T., Zuffada, C., Chao, Y., Kroger, P., Young, L.E., LaBrecque, J.L., 2002b. 5-cm-precision aircraft ocean altimetry using GPS reflections. Geophys. Res. Lett. 29 (10). https://doi.org/10.1029/2002gl014759, 13-11-13-14.

Lu, S.L., Ouyang, N.L., Wu, B.F., Wei, Y.P., Tesemma, Z., 2013. Lake water volume calculation with time series remote-sensing images. Int. J. Remote Sens. 34 (22), 7962–7973. https://doi.org/10.1080/01431161.2013.827814.

Luo, Q., Liang, Y., Guo, Y., Liang, X., Ren, C., Yue, W., Zhu, B., Jiang, X., 2023. Enhancing spatial resolution of GNSS-R soil moisture retrieval through XGBoost algorithm-based downscaling approach: A case study in the southern United States. Remote Sens. 15, 4576. https://doi.org/10.3390/rs15184576.

Ma, Z., Zhang, S., Liu, Q., Feng, Yanming, Guo, Q., Zhao, H., Feng, Yuxuan, 2024. Using CYGNSS and L-band radiometer observations to retrieve surface water fraction: A case study of the catastrophic flood of 2022 in Pakistan. IEEE Trans. Geosci. Remote Sens. 62, 1–17. https://doi.org/10.1109/TGRS.2024.3367491.

Martinis, S., Groth, S., Wieland, M., Knopp, L., Rättich, M., 2022. Towards a global seasonal and permanent reference water product from sentinel-1/2 data for

improved flood mapping. Remote Sens. Environ. 278, 113077. https://doi.org/10.1016/j.rse.2022.113077.
Martin-Neira, M., 1993. A passive reflectometry and interferometry system (PARIS): application to ocean altimetry. ESA journal. 17 (4), 331–355.
McFeeters, S.K., 1996. The use of the normalized difference water index (NDWI) in the delineation of open water features. Int. J. Remote Sens. 17 (7), 1425–1432. https://doi.org/10.1080/01431169608948714.
Mohammadimanesh, F., Salehi, B., Mahdianpari, M., Brisco, B., Motagh, M., 2018. Wetland water level monitoring using interferometric synthetic aperture radar (InSAR): A review. Can. J. Remote. Sens. 44 (4), 247–262. https://doi.org/10.1080/07038992.2018.1477680.
Moller, D., Ruf, C., Linnabary, R., O'Brien, A., Musko, S., 2021. Operational airborne GNSS-R aboard air New Zealand domestic aircraft. In: 2021 IEEE International Geoscience and Remote Sensing Symposium IGARSS. Presented at the IGARSS 2021–2021. IEEE International Geoscience and Remote Sensing Symposium, IEEE, Brussels, Belgium, pp. 1284–1287. https://doi.org/10.1109/IGARSS47720.2021.9553159.
Nash, J.E., Sutcliffe, J.V., 1970. River flow forecasting through conceptual models part I—A discussion of principles. J. Hydrol. 10, 282–290. https://doi.org/10.1016/0022-1694(70)90255-6.
Nguyen, H.H., Kim, H., Crow, W., Yueh, S., Wagner, W., Lei, F., Wigneron, J.-P., Colliander, A., Frappart, F., 2025. From theory to hydrological practice: leveraging CYGNSS data over seven years for advanced soil moisture monitoring. Remote Sens. Environ. 316, 114509. https://doi.org/10.1016/j.rse.2024.114509.
Norris, R., Ruf, C., Loria, E., O'Brien, A., 2018. Comparison of wide bandwidth conventional and interferometric GNSS-R techniques for possible CYGNSS follow-on mission. In: IGARSS 2018–2018 IEEE International Geoscience and Remote Sensing Symposium. Presented at the IGARSS 2018–2018. IEEE International Geoscience and Remote Sensing Symposium, IEEE, Valencia, pp. 4277–4280. https://doi.org/10.1109/IGARSS.2018.8517480.
Palomino-Ángel, S., Vázquez, R., Hampel, H., Anaya, J., Mosquera, P., Lyon, S.W., Jaramillo, F., 2022. Retrieval of simultaneous water-level changes in small lakes with InSAR. Geophys. Res. Lett. 49 (2). https://doi.org/10.1029/2021GL095950 e2021GL095950.
Pandey, R.K., Crétaux, J.F., Bergé-Nguyen, M., Tiwari, V.M., Drolon, V., Papa, F., Calmant, S., 2014. Water level estimation by remote sensing for the 2008 flooding of the Kosi River. Int. J. Remote Sens. 35 (2), 424–440. https://doi.org/10.1080/01431161.2013.870678.
Papa, F., Prigent, C., Durand, F., Rossow, W.B., 2006. Wetland dynamics using a suite of satellite observations: A case study of application and evaluation for the Indian subcontinent. Geophys. Res. Lett. 33 (8), L08401. https://doi.org/10.1029/2006GL025767.
Papa, F., Durand, F., Rossow, W.B., Rahman, A., Bala, S.K., 2010. Satellite altimeter-derived monthly discharge of the ganga-Brahmaputra River and its seasonal to interannual variations from 1993 to 2008. J. Geophys. Res. Oceans 115 (C12), C12013. https://doi.org/10.1029/2009jc006075.
Papadopoulos, S., Azar, E., Woon, W.-L., Kontokosta, C.E., 2018. Evaluation of tree-based ensemble learning algorithms for building energy performance estimation. J. Build. Perform. Simul. 11 (3), 322–332. https://doi.org/10.1080/19401493.2017.1354919.
Parajuli, J., Fernandez-Beltran, R., Kang, J., Pla, F., 2022. Attentional dense convolutional neural network for water body extraction from Sentinel-2 images. IEEE J. Sel. Top. Appl. Earth Obs. Remote Sens. 15, 6804–6816. https://doi.org/10.1109/Jstars.2022.3198497.
Pavelsky, T.M., Smith, L.C., 2008. RivWidth: A software tool for the calculation of river widths from remotely sensed imagery. IEEE Geosci. Remote Sens. Lett. 5 (1), 70–73. https://doi.org/10.1109/Lgrs.2007.908305.
Pavelsky, T.M., Durand, M.T., Andreadis, K.M., Beighley, R.E., Paiva, R.C.D., Allen, G.H., Miller, Z.F., 2014. Assessing the potential global extent of SWOT river discharge observations. J. Hydrol. 519, 1516–1525. https://doi.org/10.1016/j.jhydrol.2014.08.044.
Pham-Duc, B., Prigent, C., Aires, F., 2017. Surface water monitoring within Cambodia and the Vietnamese Mekong Delta over a year, with Sentinel-1 SAR observations. Water 9 (6), 366. https://doi.org/10.3390/w9060366.
Philippus, D., Sytsma, A., Rust, A., Hogue, T.S., 2024. A machine learning model for estimating the temperature of small rivers using satellite-based spatial data. Remote Sens. Environ. 311, 114271. https://doi.org/10.1016/j.rse.2024.114271.
Putatunda, S., Rama, K., 2018. A comparative analysis of hyperopt as against other approaches for hyper-parameter optimization of XGBoost. In: proceedings of the 2018 international conference on signal processing and machine learning, pp. 6–10. https://doi.org/10.1145/3297067.3297080.
Rodriguez-Alvarez, N., Podest, E., Jensen, K., McDonald, K.C., 2019. Classifying inundation in a tropical wetlands complex with GNSS-R. Remote Sens 11 (9), 1053. https://doi.org/10.3390/rs11091053.
Roesler, C.J., Morton, Y.J., Nerem, R.S., 2023. Gulf of Mexico loop-current signature observed from GNSS-R phase altimetry based on spire global CubeSat data. IEEE Trans. Geosci. Remote Sens. 61, 1–14. https://doi.org/10.1109/Tgrs.2023.3272212.
Ruf, C., Gleason, S., Jelenak, Z., Katzberg, S., Ridley, A., Rose, R., Scherrer, J., Zavorotny, V., 2012. The CYGNSS nanosatellite constellation hurricane mission, in: 2012 IEEE International Geoscience and Remote Sensing Symposium, pp. 214–216.
Ruf, C.S., Atlas, R., Chang, P.S., Clarizia, M.P., Garrison, J.L., Gleason, S., Katzberg, S.J., Jelenak, Z., Johnson, J.T., Majumdar, S.J., O'brien, A., Posselt, D.J., Ridley, A.J., Rose, R.J., Zavorotny, V.U., 2016. New Ocean winds satellite Mission to probe hurricanes and tropical convection. Bull. Am. Meteorol. Soc. 97 (3), 385–395. https://doi.org/10.1175/Bams-D-14-00218.1.
Ruf, C.S., Chew, C., Lang, T., Morris, M.G., Nave, K., Ridley, A., Balasubramaniam, R., 2018. A new paradigm in earth environmental monitoring with the CYGNSS Small satellite constellation. Sci. Rep. 8 (1), 8782. https://doi.org/10.1038/s41598-018-27127-4.
Ryan, J.C., Smith, L.C., Cooley, S.W., Pitcher, L.H., Pavelsky, T.M., 2020. Global characterization of inland water reservoirs using ICESat-2 altimetry and climate reanalysis. Geophys. Res. Lett. 47 (17). https://doi.org/10.1029/2020GL088543 e2020GL088543.
Santamaría-Gómez, A., Watson, C., 2017. Remote leveling of tide gauges using GNSS reflectometry: case study at Spring Bay. Australia. GPS Solut. 21 (2), 451–459. https://doi.org/10.1007/s10291-016-0537-x.
Santamaría-Gómez, A., Watson, C., Gravelle, M., King, M., Wöppelmann, G., 2015. Levelling co-located GNSS and tide gauge stations using GNSS reflectometry. J. Geodyn. 89 (3), 241–258. https://doi.org/10.1007/s00190-014-0784-y.
Santoro, M., Wegmüller, U., Lamarche, C., Bontemps, S., Defoumy, P., Arino, O., 2015. Strengths and weaknesses of multi-year Envisat ASAR backscatter measurements to map permanent open water bodies at global scale. Remote Sens. Environ. 171, 185–201. https://doi.org/10.1016/j.rse.2015.10.031.
Scherelis, V., Doering, M., Laube, P., 2023. HydroWidth: A small-scale approach to calculate river width and its variability. Trans. GIS 27 (5), 1503–1525. https://doi.org/10.1111/tgis.13083.
Schwatke, C., Dettmering, D., Bosch, W., Seitz, F., 2015. DAHITI - an innovative approach for estimating water level time series over inland waters using multi-mission satellite altimetry. Hydrol. Earth Syst. Sci. 19 (10), 4345–4364. https://doi.org/10.5194/hess-19-4345-2015.
Senyurek, V., Lei, F., Boyd, D., Kurum, M., Gurbuz, A.C., Moorhead, R., 2020. Machine learning-based CYGNSS soil moisture estimates over ISMN sites in CONUS. Remote Sens. 12, 1168. https://doi.org/10.3390/rs12071168.
Senyurek, V., Gurbuz, A.C., Kurum, M., 2021. Assessment of interpolation errors of CYGNSS soil moisture estimations. IEEE J. Sel. Top. Appl. Earth Observations Remote Sensing 14, 9815–9825. https://doi.org/10.1109/JSTARS.2021.3113565.
Senyurek, V., Lei, F., Gurbuz, A.C., Kurum, M., Moorhead, R., 2022. Machine learning-based global soil moisture estimation using GNSS-R. In: SoutheastCon 2022. Presented at the SoutheastCon 2022. IEEE, Mobile, AL, USA, pp. 434–435. https://doi.org/10.1109/SoutheastCon48659.2022.9764039.
Shepard, D., 1968. A two-dimensional interpolation function for irregularly-spaced data. In: proceedings of the 1968 23rd ACM national conference, pp. 517–524. https://doi.org/10.1145/800186.810616.
Shi, X.J., Chen, Z.R., Wang, H., Yeung, D.Y., Wong, W.K., Woo, W.C., 2015. Convolutional LSTM network: A machine learning approach for precipitation Nowcasting. In, advances in neural information processing systems 28 (nips 2015).
Song, L.J., Song, C.Q., Luo, S.X., Chen, T., Liu, K., Zhang, Y.L., Ke, L.H., 2023. Integrating ICESat-2 altimetry and machine learning to estimate the seasonal water level and storage variations of national-scale lakes in China. Remote Sens. Environ. 294, 113657. https://doi.org/10.1016/j.rse.2023.113657.
Sulistioadi, Y.B., Tseng, K.H., Shum, C.K., Hidayat, H., Sumaryono, M., Suhardiman, A., Setiawan, F., Sunarso, S., 2015. Satellite radar altimetry for monitoring small rivers and lakes in Indonesia. Hydrol. Earth Syst. Sci. 19 (1), 341–359. https://doi.org/10.5194/hess-19-341-2015.
Tarpanelli, A., Santi, E., Tourian, M.J., Filippucci, P., Amarnath, G., Brocca, L., 2018. Daily river discharge estimates by merging satellite optical sensors and radar altimetry through artificial neural network. IEEE Trans. Geosci. Remote Sens. 57 (1), 329–341. https://doi.org/10.1109/TGRS.2018.2854625.
Treuhaft, R.N., Lowe, S.T., Zuffada, C., Chao, Y., 2001. 2-cm GPS altimetry over crater Lake. Geophys. Res. Lett. 28 (23), 4343–4346. https://doi.org/10.1029/2001gl013815.
Unwin, M.J., Pierdicca, N., Cardellach, E., Rautiainen, K., Foti, G., Blunt, P., Guerriero, L., Santi, E., Tossaint, M., 2021. An introduction to the HydroGNSS GNSS reflectometry remote sensing mission. IEEE J. Sel. Top. Appl. Earth Observ. Remote Sens. 14, 6987–6999. https://doi.org/10.1109/JSTARS.2021.3089550.
Vanthof, V., Kelly, R., 2019. Water storage estimation in ungauged small reservoirs with the TanDEM-X DEM and multi-source satellite observations. Remote Sens. Environ. 235, 111437. https://doi.org/10.1016/j.rse.2019.111437.
Verma, U., Chauhan, A., Pai, M.M.M., Pai, R., 2021. DeepRivWidth : deep learning based semantic segmentation approach for river identification and width measurement in SAR images of coastal Karnataka. Comput. Geosci. 154, 104805. https://doi.org/10.1016/j.cageo.2021.104805.
Wang, X.L., Zhang, Q., Zhang, S.C., 2018. Water levels measured with SNR using wavelet decomposition and Lomb-Scargle periodogram. GPS Solutions 22 (1), 1–10. https://doi.org/10.1007/s10291-017-0684-8.
Wang, X.L., He, X.F., Zhang, Q., 2019a. Evaluation and combination of quad-constellation multi-GNSS multipath reflectometry applied to sea level retrieval. Remote Sens. Environ. 231, 111229. https://doi.org/10.1016/j.rse.2019.111229.
Wang, X.L., Zhang, Q., Zhang, S.C., 2019b. Sea level estimation from SNR data of geodetic receivers using wavelet analysis. GPS Solutions 23 (1), 1–14. https://doi.org/10.1007/s10291-018-0798-7.
Wang, X., He, X., Xiao, R., Song, M., Jia, D., 2021. Millimeter to centimeter scale precision water-level monitoring using GNSS reflectometry: application to the south-to-north water diversion project. China. Remote Sens. Environ. 265, 112645. https://doi.org/10.1016/j.rse.2021.112645.
Wang, Q.M., Tang, Y.J., Tong, X.H., Atkinson, P.M., 2024. Filling gaps in cloudy Landsat LST product by spatial-temporal fusion of multi-scale data. Remote Sens. Environ. 306, 114142. https://doi.org/10.1016/j.rse.2024.114142.
Weekley, D., Li, X.G., 2021. Tracking lake surface elevations with proportional hypsometric relationships, Landsat imagery, and multiple DEMs. Water Resour. Res. 57 (1). https://doi.org/10.1029/2020WR027666 e2020WR027666.

Wei, Z., Miao, L., Peng, J., Zhao, T., Meng, L., Lu, H., Peng, Z., Cosh, M.H., Fang, B., Lakshmi, V., Shi, J., 2024. Bridging spatio-temporal discontinuities in global soil moisture mapping by coupling physics in deep learning. Remote Sens. Environ. 313, 114371. https://doi.org/10.1016/j.rse.2024.114371.

Wu, Q., Ke, L., Wang, J., Pavelsky, T.M., Allen, G.H., Sheng, Y., Duan, X., Zhu, Y., Wu, J., Wang, L., 2023. Satellites reveal hotspots of global river extent change. Nat. Commun. 14 (1), 1587. https://doi.org/10.1038/s41467-023-38302-1.

Xi, R.J., Qin, Y., Jiang, W.P., Zhou, X.H., Xu, D.S., Fan, X.C., 2022. Water level retrieval using a posteriori residual of GNSS Pseudorange and carrier-phase observations. IEEE Trans. Geosci. Remote Sens. 60, 1–13. https://doi.org/10.1109/Tgrs.2022.3188332.

Xiao, Z.B., Wang, Y., Fu, K., Wu, F., 2017. Identifying different transportation modes from trajectory data using tree-based ensemble classifiers. ISPRS Int. J. Geo Inf. 6 (2), 57. https://doi.org/10.3390/ijgi6020057.

Xing, L., Tang, X., Wang, H., Fan, W., Wang, G., 2018. Monitoring monthly surface water dynamics of Dongting Lake using Sentinel-1 data at 10 m. PeerJ 6, e4992. https://doi.org/10.7717/peerj.4992.

Xu, N., Ma, Y., Zhang, W.H., Wang, X.H., Yang, F.L., Su, D.P., 2020. Monitoring annual changes of Lake water levels and volumes over 1984-2018 using Landsat imagery and ICESat-2 data. Remote Sens. 12 (23), 4004. https://doi.org/10.3390/rs12234004.

Xue, W., Yang, H., Wu, Y., Kong, P., Xu, H., Wu, P., Ma, X., 2021. Water body automated extraction in polarization SAR images with dense-coordinate-feature-concatenate network. IEEE J. Sel. Topics Appl. Earth Observ. Remote Sens. 14, 12073–12087. https://doi.org/10.1109/JSTARS.2021.3129182.

Xue, Y., Qin, C., Wu, B.S., Li, D., Fu, X.D., 2022. Automatic extraction of Mountain River surface and width based on multisource high-resolution satellite images. Remote Sens. 14 (10), 2370. https://doi.org/10.3390/rs14102370.

Yan, Q.Y., Huang, W.M., Jin, S.G., Jia, Y., 2020. Pan-tropical soil moisture mapping based on a three-layer model from CYGNSS GNSS-R data. Remote Sens. Environ. 247, 111944. https://doi.org/10.1016/j.rse.2020.111944.

Yang, X., Qin, Q., Grussenmeyer, P., Koehl, M., 2018. Urban surface water body detection with suppressed built-up noise based on water indices from Sentinel-2 MSI imagery. Remote Sens. Environ. 219. https://doi.org/10.1016/j.rse.2018.09.016.

Yang, X., Pavelsky, T.M., Allen, G.H., Donchyts, G., 2020. RivWidthCloud: an automated Google earth engine algorithm for river width extraction from remotely sensed imagery. IEEE Geosci. Remote Sens. Lett. 17 (2), 217–221. https://doi.org/10.1109/LGRS.2019.2920225.

Ye, M.D., Jin, S.G., Jia, Y., 2022. Ten-Minute Sea-level variations from combined multi-GNSS multipath reflectometry based on a weighted iterative Least-Square method. IEEE Trans. Geosci. Remote Sens. 60, 1–10. https://doi.org/10.1109/Tgrs.2022.3194033.

Young, C.-C., Cheng, Y.-C., Lee, M.-A., Wu, J.-H., 2024. Accurate reconstruction of satellite-derived SST under cloud and cloud-free areas using a physically-informed machine learning approach. Remote Sens. Environ. 313, 114339. https://doi.org/10.1016/j.rse.2024.114339.

Yue, L.W., Zan, F.Q., Liu, X.G., Yuan, Q.Q., Shen, H.F., 2022. The Spatio-temporal reconstruction of Lake water levels using deep learning models: A case study on Altai Mountains. IEEE J. Sel. Top. Appl. Earth Obs. Remote Sens. 15, 4919–4940. https://doi.org/10.1109/Jstars.2022.3182646.

Yueh, S.H., Shah, R., Chaubell, M.J., Hayashi, A., Xu, X., Colliander, A., 2022. A semiempirical modeling of soil moisture, vegetation, and surface roughness impact on CYGNSS reflectometry data. IEEE Trans. Geosci. Remote Sensing 60, 1–17. https://doi.org/10.1109/TGRS.2020.3035989.

Zeiger, P., Frappart, F., Darrozes, J., Prigent, C., Jiménez, C., 2022. Analysis of CYGNSS coherent reflectivity over land for the characterization of pan-tropical inundation dynamics. Remote Sens. Environ. 282, 113278. https://doi.org/10.1016/j.rse.2022.113278.

Zhang, J.H., Morton, A.D., 2023. Inland water body surface height retrievals using CYGNSS delay Doppler maps. IEEE Trans. Geosci. Remote Sens. 61, 1–16. https://doi.org/10.1109/Tgrs.2023.3330410.

Zhang, G.Q., Xie, H.J., Kang, S.C., Yi, D.H., Ackley, S.F., 2011. Monitoring lake level changes on the Tibetan plateau using ICESat altimetry data (2003-2009). Remote Sens. Environ. 115 (7), 1733–1742. https://doi.org/10.1016/j.rse.2011.03.005.

Zhang, J., Morton, Y.J., Wang, Y., Roesler, C.J., 2022. Mapping surface water extents using high-rate coherent spaceborne GNSS-R measurements. IEEE Trans. Geosci. Remote Sensing 60, 1–15. https://doi.org/10.1109/TGRS.2022.3218254.

Zhao, W.Z., Qu, Y., Chen, J.G., Yuan, Z.L., 2020. Deeply synergistic optical and SAR time series for crop dynamic monitoring. Remote Sens. Environ. 247, 111952. https://doi.org/10.1016/j.rse.2020.111952.

Zhou, H.W., Liu, S.X., Mo, X.G., Hu, S., Zhang, L., Ma, J., Bandini, F., Grosen, H., Bauer-Gottwein, P., 2023. Calibrating a hydrodynamic model using water surface elevation determined from ICESat-2 derived cross-section and Sentinel-2 retrieved sub-pixel river width. Remote Sens. Environ. 298, 113796. https://doi.org/10.1016/j.rse.2023.113796.

Zhu, X.L., Chen, J., Gao, F., Chen, X.H., Masek, J.G., 2010. An enhanced spatial and temporal adaptive reflectance fusion model for complex heterogeneous regions. Remote Sens. Environ. 114 (11), 2610–2623. https://doi.org/10.1016/j.rse.2010.05.032.